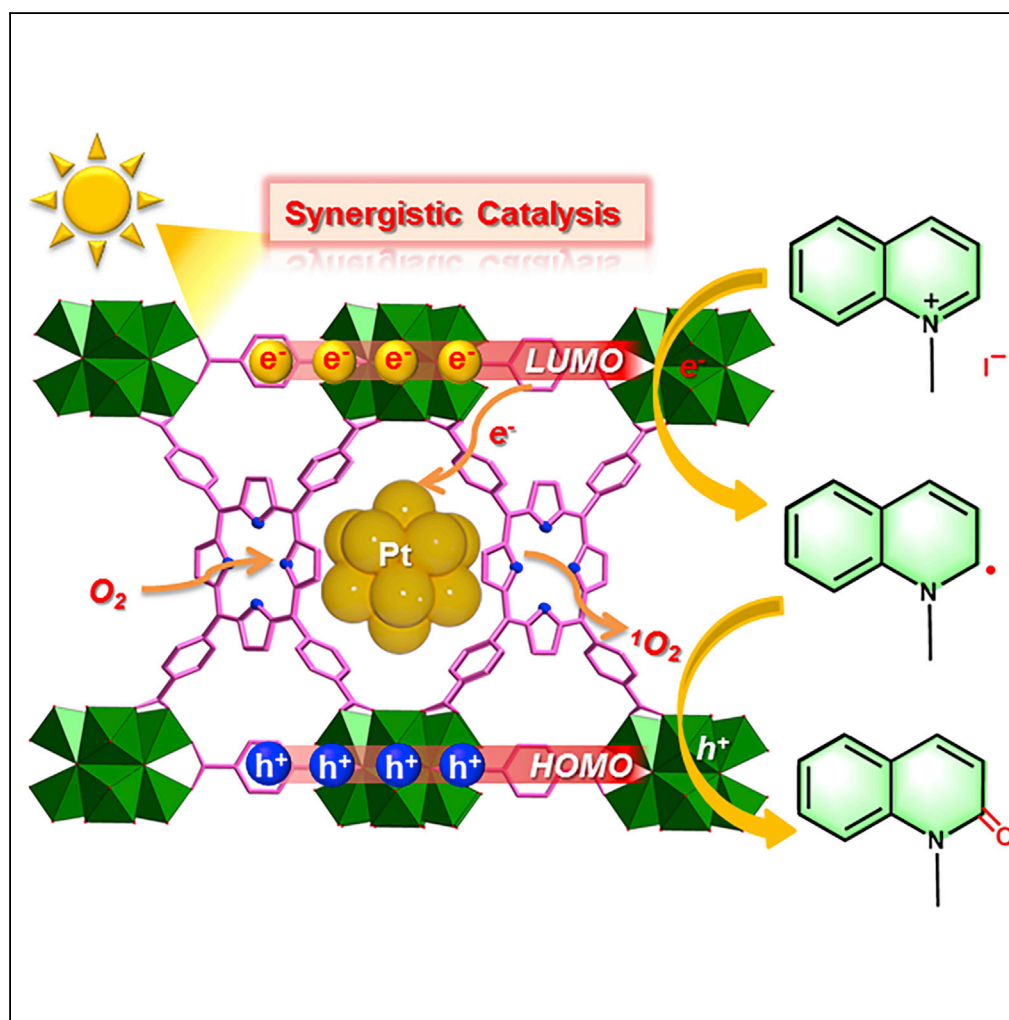


Article

Synergistic Effect over Sub-nm Pt Nanocluster@MOFs Significantly Boosts Photo-oxidation of *N*-alkyl(iso)quinolinium Salts

Shan-Shan Fu, Xiu-Ying Ren, Song Guo, Guangxu Lan, Zhi-Ming Zhang, Tong-Bu Lu, Wenbin Lin

guosong@email.tjut.edu.cn (S.G.)
zmzhang@email.tjut.edu.cn (Z.-M.Z.)

HIGHLIGHTS

A state-of-the-art photocatalyst for preparation of bioactive (iso)quinolones

Synergistic catalysis of photogenerated e^-/h^+ and 1O_2

Sub-nm $Pt_{0.9}@PCN-221$ with a high efficiency of e^-/h^+ separation and 1O_2 generation

Article

Synergistic Effect over Sub-nm Pt Nanocluster@MOFs Significantly Boosts Photo-oxidation of *N*-alkyl(iso)quinolinium Salts

Shan-Shan Fu,¹ Xiu-Ying Ren,² Song Guo,^{1,*} Guangxu Lan,³ Zhi-Ming Zhang,^{1,2,4,*} Tong-Bu Lu,¹ and Wenbin Lin³

SUMMARY

Quinolones and isoquinolones are of interest to pharmaceutical industry owing to their potent biological activities. Herein, we first encapsulated sub-nm Pt nanoclusters into Zr-porphyrin frameworks to afford an efficient photocatalyst Pt_{0.9}@PCN-221. This catalyst can dramatically promote electron-hole separation and ¹O₂ generation to achieve synergistic effect first in the metal-organic framework (MOF) system, leading to the highest activity in photosynthesis of (iso)quinolones in >90.0% yields without any electronic sacrificial agents. Impressively, Pt_{0.9}@PCN-221 was reused 10 times without loss of activity and can catalyze gram-scale synthesis of 1-methyl-5-nitroisoquinolinone at an activity of 175.8 g·g_{cat}⁻¹, 22 times higher than that of PCN-221. Systematic investigations reveal the contribution of synergistic effect of photogenerated electron, photogenerated hole, and ¹O₂ generation for efficient photo-oxidation, thus highlighting a new strategy to integrate multiple functional components into MOFs to synergistically catalyze complex photoreactions for exploring biologically active heterocyclic molecules.

INTRODUCTION

Quinolones and isoquinolones are important drug candidates due to their potent biological effects (Glushkov and Shklyayev, 2001; Carey et al., 2006; Claassen et al., 2009; Forbis and Rinehart, 1973). For instance, quinolones exhibited strong anticancer and antibiotic activities (Forbis and Rinehart, 1973; Ni et al., 2006), whereas isoquinolones have been used to treat stomach cancer and brain tumors (Glushkov and Shklyayev, 2001). As a result, significant efforts have been devoted to the synthesis of (iso)quinolones from readily available *N*-alkyl(iso)quinolinium salts (Fan-Chiang et al., 2016; Ishi-i et al., 2010; Khalil et al., 2016; Wang et al., 2016; Luo et al., 2016; Jin et al., 2017). A number of catalysts, including K₃Fe(CN)₆ (Fan-Chiang et al., 2016; Ishi-i et al., 2010; Khalil et al., 2016), copper (Wang et al., 2016), iodine (Luo et al., 2016), and eosin Y (Jin et al., 2017), have been used to convert *N*-alkyl(iso)quinolinium salts to (iso)quinolones. However, the practical application of these catalysts is limited by their potential toxicity, high energy consumption, poor functional group tolerance, and the difficulty in catalyst recycle and reuse. More environment-friendly heterogeneous catalysts with a broad substrate scope are needed for the facile synthesis of (iso)quinolones.

Metal-organic frameworks (MOFs) have shown great potential in photocatalytic reactions by virtue of their well-defined structures, porosity, and the ability to incorporate multiple functionalities (Zhang et al., 2017a, 2017b; Wu et al., 2012; Chen et al., 2019; Liu et al., 2014; Wu and Zhao, 2017; Ji et al., 2017; Dhakshinamoorthy et al., 2018; Xia et al., 2017; Aijaz and Xu, 2014; Lee et al., 2009; Pascanu et al., 2019; Yang and Wang, 2018; Zhou et al., 2012; Saha et al., 2014; Luo et al., 2019). In particular, MOFs have provided a versatile platform to introduce multiple components, such as photosensitizers (PSs) and catalysts, for efficient conversion of solar energy via synergistic catalysis (Deng et al., 2017; Dhakshinamoorthy et al., 2018; Muzzio et al., 2019; Sun and Li, 2016; Wang and Li, 2016; Wu and Zhao, 2017; Xia et al., 2017; Yang et al., 2017). With their excellent stability and tailorability, Zr-based MOFs have been widely studied for artificial photosynthesis (Abdel-Mageed et al., 2019; Bai et al., 2016a; Chen et al., 2017; Howarth et al., 2016; Kandiah et al., 2010; Liu et al., 2018; Wang et al., 2012) and photocatalytic organic reactions (Wang et al., 2012; Paille et al., 2018; Sun et al., 2018; Xu et al., 2015) by hierarchical integration of PSs and catalysts to accelerate electron transfer and promote the separation of photogenerated electron-hole pairs (Choi et al., 2017; Paille et al., 2018; Pullen et al., 2013; Xiao et al., 2016; Yang et al., 2017; Zhang et al., 2015). However, most studies to date have focused on oxidation or reduction half-reactions in the presence of sacrificial agents (Wang et al., 2012; Xiao et al., 2016). New and exciting approaches are merging with the goal of exploiting cooperative

¹Institute for New Energy Materials and Low Carbon Technologies, School of Materials Science and Engineering, Tianjin University of Technology, Tianjin 300384, China

²College of Chemistry, Northeast Normal University, Changchun 130024, P.R. China

³Department of Chemistry, University of Chicago, 929 East 57th Street, Chicago, IL 60637, USA

⁴Lead Contact

*Correspondence: guosong@email.tjut.edu.cn (S.G.), zmzhang@email.tjut.edu.cn (Z.-M.Z.)

<https://doi.org/10.1016/j.isci.2019.100793>



effects between photogenerated electrons and holes to further enhance the efficacy of photocatalytic organic reactions (Liu et al., 2018; Paille et al., 2018; Wu et al., 2019).

Noble metal nanoparticles are known to efficiently trap electrons migrated from an n-type semiconductor. This Schottky effect effectively separates photogenerated electrons and holes. Electron-rich Pt nanoparticles can also activate O_2 to form singlet oxygen (1O_2), which exhibits high activity in oxidation reactions (Chen et al., 2017). We hypothesize that the encapsulation of Pt nanoparticles into Zr-based MOFs can not only enhance the separation of photoexcited electron-hole pairs but also boost 1O_2 generation, leading to synergistic activation of organic substrates for difficult transformations.

Herein, we demonstrate for the first-time synergistic combination of photoexcited electron-hole pairs with 1O_2 generated on sub-nm Pt nanoclusters (NCs) in an ultrafine Pt NC-encapsulated Zr-porphyrin MOF for photocatalytic oxidation of *N*-alkyl(iso)quinolinium salts to (iso)quinolones (Figures S1–S26). The sizes of Pt NCs in the MOF matrix were precisely controlled from sub-nm to 3 nm by *in situ* photoreduction of K_2PtCl_4 to afford a family of heterogeneous photocatalysts $Pt_x@PCN-221$ (where $x = 0.9, 1.6, 2.2,$ and 3.0 nm) with Pt NC size-dependent photocatalytic activities. For photocatalytic oxidation of *N*-alkylquinolinium salts, $Pt_{0.9}@PCN-221$ shows the best catalytic activity among all these composite catalysts to produce quinolones in >90.0% yield after 2 h of visible light irradiation. $Pt_{0.9}@PCN-221$ was reused 10 times without loss of activity and catalyzed photo-oxidation of 1-methyl-5-nitrosoquinolinium iodide in gram scale in 6 h to afford 1-methyl-5-nitrosoquinolinone at an activity of $175.8 \text{ g} \cdot \text{g}_{\text{cat}}^{-1}$, which is 22 times higher than that of PCN-221. A series of spectroscopic and quenching studies revealed the role of synergistic electron-hole separation and 1O_2 generation in achieving the extremely high activity of photocatalytic *N*-alkyl (iso)quinolinium by the sub-nm Pt NC@MOF composite.

RESULTS

Synthesis and Characterization

Ultrafine Pt NCs were loaded into Zr-based porphyrin MOF (PCN-221) by *in situ* photoreduction of K_2PtCl_4 via an intermittent illumination process (Figure 1A). In this process, the sizes of MOF-encapsulated Pt NCs were readily tuned from sub-nm to 3.0 nm by controlling the loading amount of K_2PtCl_4 and the irradiation time. Sub-nm Pt NCs were obtained with a low K_2PtCl_4 loading of 9.2 mg in 14.0 mg PCN-221 and a short irradiation time of 6 s (interval of dark time of 54 s) for 20 cycles with a total irradiation time of 120 s. By increasing the total irradiation time to 360 s, 1.6-nm Pt NCs were obtained with the same K_2PtCl_4 loading; 3.0-nm Pt NCs were synthesized by increasing the K_2PtCl_4 loading to 18.3 mg with a total irradiation time to 360 s (Figure 1).

High-resolution scanning electron microscopic images of both PCN-221 and $Pt_x@PCN-221$ showed an irregular octahedral shape (Figure S27). Powder X-ray diffraction of $Pt_x@PCN-221$ samples exhibited identical patterns to that simulated for PCN-221, indicating that the structure and crystallinity of PCN-221 are maintained upon encapsulating Pt NCs (Figure 1D). It is worth noting that no diffraction peaks from Pt NCs were detected, likely as a result of ultrafine Pt NCs inside the PCN-221 framework. Taking $Pt_{1.6}@PCN-221$ as an example, high-resolution transmission electron microscopic studies revealed that all NCs uniformly distribute in the PCN-221 skeleton with an average size of 1.6 nm (Figure S28E). To further clarify the structure of Pt NCs, $Pt_x@PCN-221$ samples were calcined at 500°C to transform organic components in the MOF into N-doping porous carbon (N-C) (Cao et al., 2017), and Zr was removed from the support with HF acid etching to eliminate the interference of Zr in high-angle annular dark-field imaging scanning transmission electron microscopic (HAADF-STEM) imaging studies (Figures 1B and S28–S30). The content of Pt was determined as 2.83% and 2.81% before and after the removal of Zr, respectively. Pt NCs were clearly visible on the N-C support, and their average sizes are determined as 0.9, 1.6, 2.2, and 3.0 nm, respectively, with a narrow size distribution (Figures 1B and S29). Energy-dispersive X-ray spectroscopic elemental mapping showed that N, C, and O were homogeneously distributed around N-C, whereas Pt clusters were clearly observed on the N-C support (Figure 1C). In addition, the diameter of polyhedral cages of PCN-221 was ~ 2.0 nm, which was smaller than that of 2.2 and 3.0 nm Pt NCs. This can be attributed to partial MOF framework distortion during Pt NC formation. Moreover, the diameter of the cage opening was around 0.8 nm, manifesting that 0.9-nm Pt NCs can be trapped into PCN-221.

In addition, the loadings of Pt were determined as 2.59% in $Pt_{0.9}@PCN-221$, 2.79% in $Pt_{1.6}@PCN-221$, 1.15% in $Pt_{2.2}@PCN-221$, and 8.43% in $Pt_{3.0}@PCN-221$, by inductively coupled plasma-mass spectrometry. N_2 sorption isotherms at 77 K showed that the pore diameter and pore volumes of $Pt_x@PCN-221$ composites are much smaller than those of pristine PCN-221, consistent with the encapsulation of Pt NCs in the cages of the MOFs

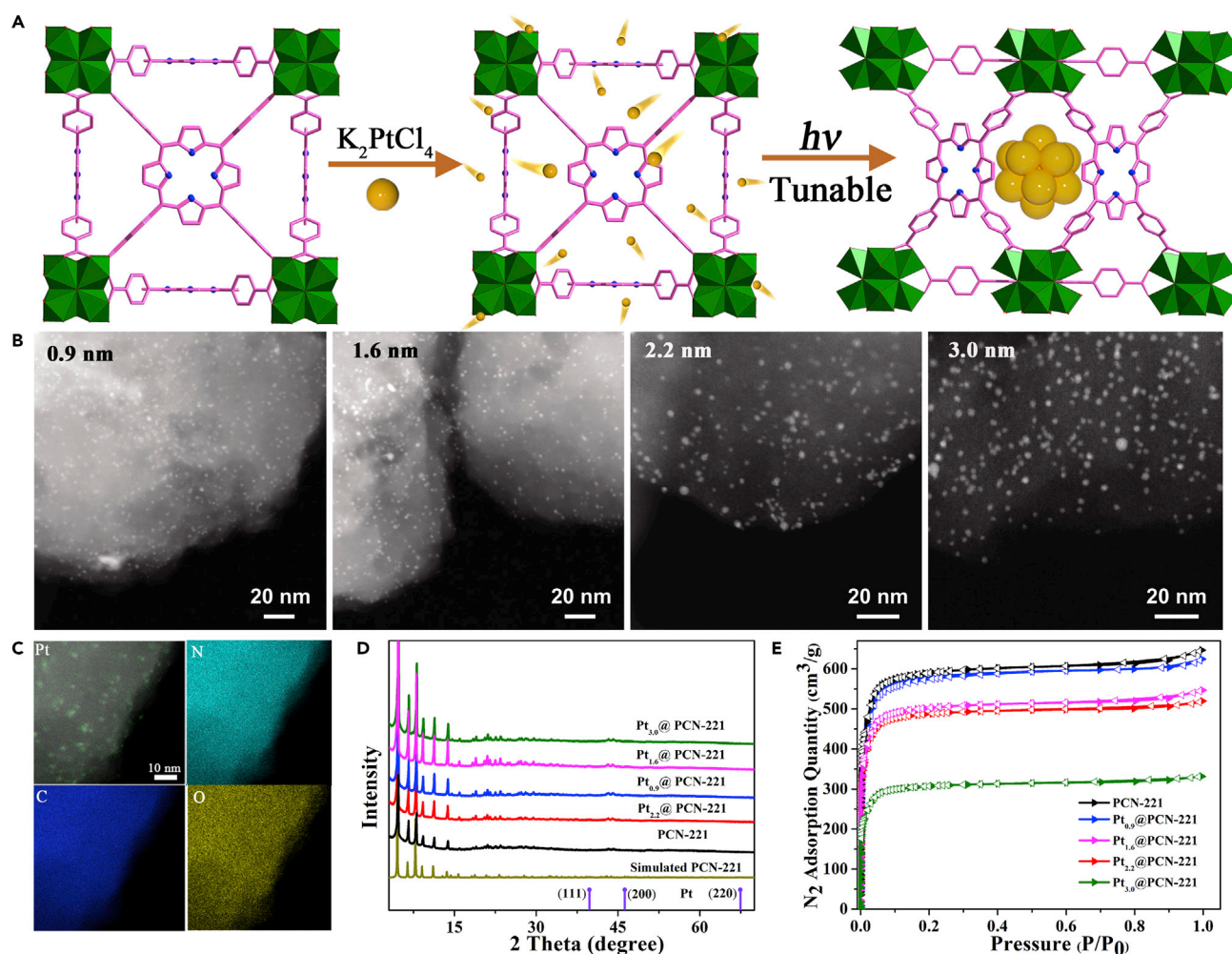


Figure 1. Preparation and Structure Characterization of Pt_x@PCN-221 and Pt_x@N-C

(A) Schematic illustration of the preparation of Pt_x@PCN-221 composites with different sizes of Pt NCs.

(B) High-angle annular dark-field scanning transmission electron microscopy (HAADF-STEM) images of Pt_x@N-C with different sizes of Pt NCs; hundreds of NCs were counted to get the size distribution.

(C) Elemental mapping images of Pt_{0.9}@N-C corresponding to Pt, C, N, and O elements, respectively.

(D) Simulated and experimental PXRD patterns of Pt nanoparticles, PCN-221, and Pt_x@PCN-221 composites.

(E) N₂ adsorption-desorption isotherms of Pt_x@PCN-221 obtained at 77 K.

(Figure 1E) (Chen et al., 2019). Among these composites, Pt_{0.9}@PCN-221 exhibits larger Brunauer-Emmett-Teller surface area and pore volume than other composites with larger particle size Pt NCs (Table S1).

Separation of Photogenerated Electron-Hole Pairs

Efficient electron-hole separation is key to realizing photocatalytic reactions (Xiao and Jiang, 2019; Kong et al., 2018). The charge separation efficiency of different Pt_x@PCN-221 samples was studied in detail by absorption spectroscopy and photoluminescence (PL) spectroscopy (Figures 2 and S31). UV-visible spectra of Pt_x@PCN-221 composites showed essentially the same absorption features in the 300–700 nm range as PCN-221. With decreasing size of Pt NCs, the scattering at >700 nm becomes weaker, likely due to spatial separation between the MOF skeleton and small NCs (Xiao et al., 2016; Sarina et al., 2014). PL spectroscopy provided important insights into the photo-induced charge transfer processes in Pt_x@PCN-221 (Sun et al., 2018). The steady-state PL intensity decreased in the order PCN-221 > Pt_{3.0}@PCN-221 > Pt_{1.6}@PCN-221 > Pt_{0.9}@PCN-221, indicating that the manipulation of Pt-MOF interactions by reducing the size of NCs can efficiently suppress the radiative electron-hole recombination process. Pt_{0.9}@PCN-221 showed the highest efficiency of charge separation among all the samples. Furthermore, the photogenerated charge

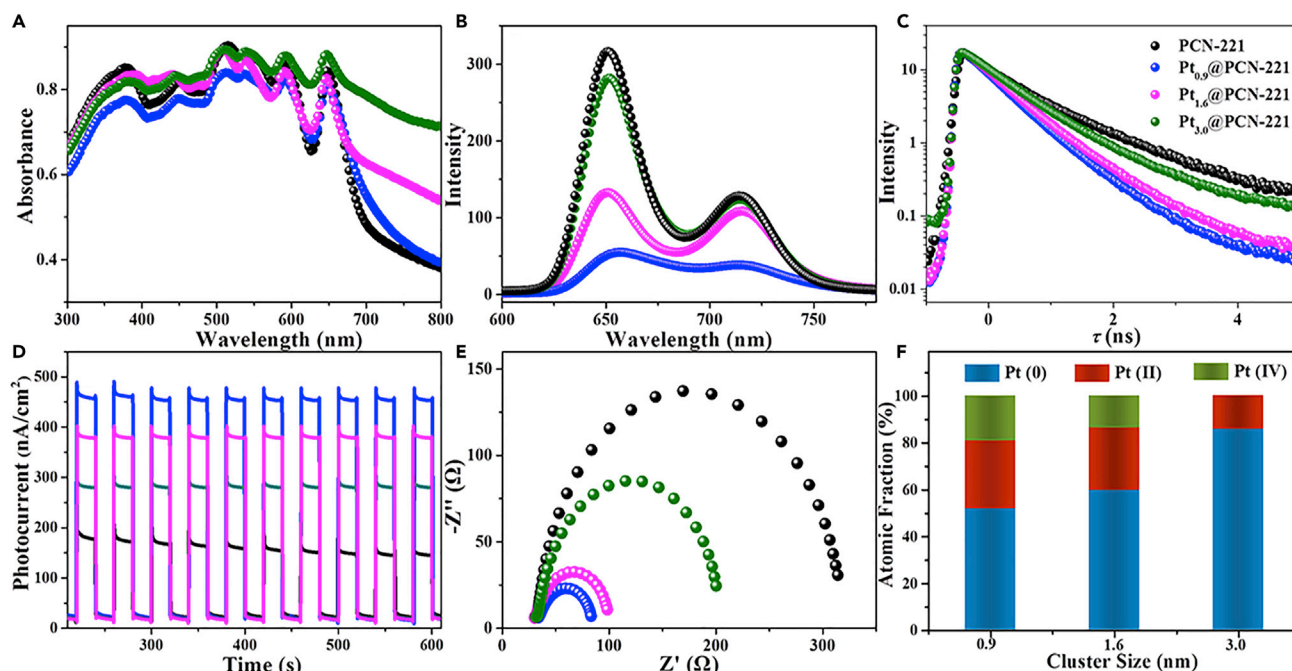


Figure 2. Photogenerated Electron-Hole Separation of Composites

(A) UV-visible diffuse reflectance spectra.

(B) PL emission spectra (excited at 410 nm).

(C) Time-resolved photoluminescence decays of PCN-221 and $Pt_x@PCN-221$.

(D and E) (D) Photocurrent responses and (E) electrochemical impedance spectroscopy Nyquist plots for PCN-221 (black), $Pt_{0.9}@PCN-221$ (blue), $Pt_{1.6}@PCN-221$ (magenta), and $Pt_{3.0}@PCN-221$ (olive).

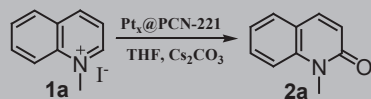
(F) Oxidation state distribution of Pt determined by X-ray photoelectron spectroscopy measurements of Pt NCs with various sizes.

separation dynamics was investigated by time-resolved PL (Figure 2C). The luminescence lifetime of $Pt_x@PCN-221$ became shorter than that of PCN-221 composite, indicating an efficient electron transfer from PCN-221 to Pt NCs. As the size of Pt NCs decreased, the decay became faster, manifesting that ultrafine Pt NCs greatly contributed to the separation of photogenerated electron and hole. These observations were supported by photocurrent measurements (Figure 2D). The photocurrent of the composite becomes larger with the decreasing size of Pt NCs, indicating that ultrafine NCs, especially for sub-nm NCs, can efficiently extract electrons from photoexcited PCN-221. In addition, electrochemical impedance spectroscopy results revealed that the radius of capacity impedance correlates with the size of NCs. $Pt_{0.9}@PCN-221$ exhibits the smallest radius, implying its lowest charge transfer resistance when compared with other composites. All these results indicate that $Pt_{0.9}@PCN-221$ possesses the highest efficiency of photo-induced electron-hole separation among the $Pt_x@PCN-221$ samples.

X-ray photoelectron spectroscopy was used to determine the valence states of Pt NCs with different sizes (Figure S32) (Wang et al., 2013). As shown Figure 2F, Pt NCs show a combination of three valence states of Pt^0 , Pt^{2+} , and Pt^{4+} . The ratio of high-valence Pt centers increased with decreasing Pt NC particle size (Bai et al., 2016b; Wang et al., 2013). The smaller Pt NCs with more high-valence Pt centers possess better ability to accept electron from excited PCN-221, which can promote photogenerated electron-hole separation of PCN-221. The electron-rich Pt NCs will facilitate 1O_2 generation (Chen et al., 2017). As a result, the enhanced efficiency of charge separation for small Pt NCs can thus be attributed to two reasons. (1) Proximity between ultrafine Pt NCs and the MOF framework facilitates electron injection from photoexcited PCN-221 to Pt NCs. (2) Higher-valence Pt centers in smaller Pt NCs endow them with stronger ability to extract electrons from photoexcited PCN-221, which can promote the photocatalytic activity.

Photo-oxidation of N-Alkyl(iso)quinolinium Salts

We next examined the photocatalytic activity of $Pt_x@MOF$ composites with different cluster sizes. In a typical photocatalytic reaction, 2 mg $Pt_x@MOF$ was used to catalyze the oxidation of 0.4 mmol



Entry	Catalyst	t/h	Yield/% ^a
1	PCN-221	2	25.6
2 ^b	Pt _{0.9} @PCN-221	2	92.8
3 ^c	Pt _{0.9} @PCN-221	2	91.5
4 ^d	Pt _{0.9} @PCN-221	2	64.3
5 ^e	Pt _{0.9} @PCN-221	2	41.5
3 ^b	Pt _{1.6} @PCN-221	2	83.6
4 ^b	Pt _{2.2} @PCN-221	2	30.1
5 ^b	Pt _{3.0} @PCN-221	2	55.3
6 ^b	Pt _{0.9} @PCN-221	6 (14)	54.5 (86.3) ^f
7 ^b	PCN-221	6 (14)	2.4 (5.3) ^f

Table 1. Visible-Light-Driven Aerobic Oxidation of 1-Methylquinolinium Iodide (1a) to 1-Methyl-2-quinolinone (2a) with Pt_x@PCN-221 as Catalysts

Reaction conditions: **1a** (0.4 mmol); photocatalysts (2 mg) with 0.068 mol %, 0.073 mol %, 0.030 mol %, and 0.22 mol % Pt versus **1a** for Pt_{0.9}@PCN-221, Pt_{1.6}@PCN-221, Pt_{2.2}@PCN-221, and Pt_{3.0}@PCN-221, respectively; Cs₂CO₃ (0.6 mmol); THF (4 mL); air; room temperature; irradiation with 425-nm LED in a 5-mL glass tube.

^aIsolated yield.

^bCs₂CO₃.

^cK₂CO₃.

^dK₃PO₄.

^eNa₂CO₃.

^fReaction conditions: **1b** (1 g), 2 mg Pt_{0.9}@PCN-221 (0.0084 mol% Pt versus **1b**), Cs₂CO₃ (0.9 mmol), THF (6 mL), air, room temperature, irradiation with 425-nm LED.

N-methylquinolinium iodide or *N*-alkylisoquinoline salts in tetrahydrofuran (THF) (4 mL) in the presence of 0.6 mmol Cs₂CO₃ with irradiation by a 425-nm light-emitting diode. As shown in Table 1, the decreasing size of Pt NCs increased the photocatalytic performance; the yield for the quinolinone product increased from 55.3% for Pt_{3.0}@PCN-221 to 92.8% for Pt_{0.9}@PCN-221 in 2 h. This photocatalytic activity is much enhanced compared with that of PCN-221 (25.6%). To optimize the condition, the catalytic performance using Cs₂CO₃, K₂CO₃, K₃PO₄, and Na₂CO₃ as bases were compared under similar condition (Table 1). These results indicate that the photocatalytic activity with Cs₂CO₃ is much better than that with other bases. It should be noted that the lower yield of Pt_{2.2}@PCN-221 compared with Pt_{0.9}@PCN-221 could be attributed to its low content of Pt. Furthermore, no quinolinone was detected without light irradiation or in the absence of air, indicating that both of them are necessary for the photo-oxidation of *N*-methylquinolinium iodide. Consistent with this, photo-oxidation reaction in oxygen atmosphere further increased the quinolinone yield to 95.8%. As Pt_{0.9}@PCN-221 was the most efficient catalyst among the composites, it was used for subsequent studies. In addition, the photocatalytic experiments were also performed with the same amount of Pt for comparing the mass-specific activity of Pt in these composites (Table S2). Their photocatalytic activities were in the order of Pt_{0.9}@PCN-221 > Pt_{1.6}@PCN-221 > Pt_{2.2}@PCN-221 > Pt_{3.0}@PCN-221, highlighting that Pt_{0.9}@PCN-221 represents the most efficient photocatalyst for photo-oxidation of *N*-alkyl(iso)quinolinium salts among these composites.

We further showed that Pt_{0.9}@PCN-221 could be reused by simple centrifugation without further activation and its photocatalytic activity remained constant for 10 cycles (Figures 3 and S33A) (Liu et al., 2019). HAADF-STEM imaging further revealed that the sizes of Pt NCs remained around 0.9 nm after five cycles of photocatalytic reactions (Figures 3C and 3D). PXRD pattern and shape of Pt_{0.9}@PCN-221 also remained unchanged after photocatalytic reactions (Figures 3B and S27). These results indicate that Pt_{0.9}@PCN-221 is

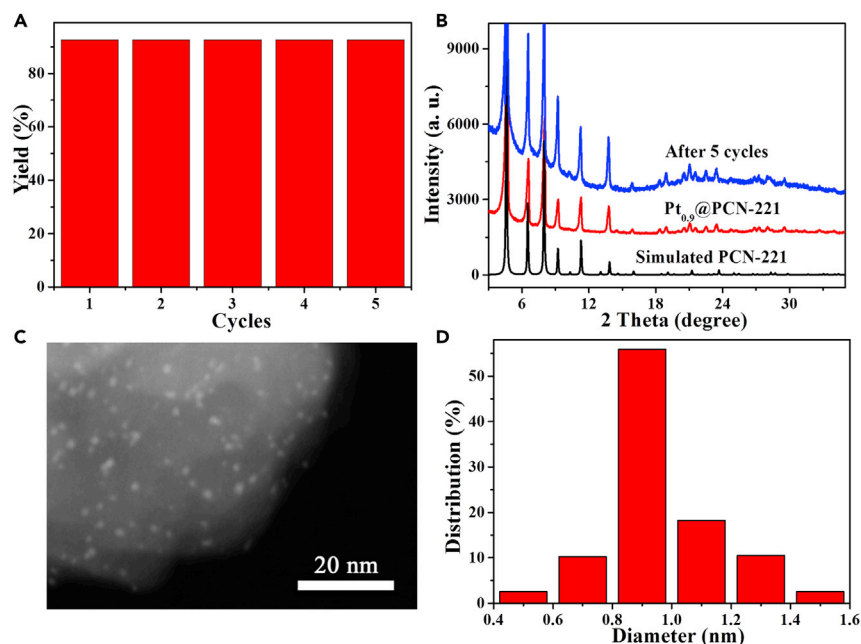


Figure 3. Recyclability of $Pt_{0.9}@PCN-221$

(A) Recyclability of $Pt_{0.9}@PCN-221$ for photo-oxidation of 1a.

(B) Predicted and experimental PXRD patterns of $Pt_{0.9}@PCN-221$ before and after the catalytic reaction.

(C and D) (C) HAADF-STEM image and (D) size distributions of Pt NCs after catalytic reaction; hundreds of NCs were counted to get the distribution.

a robust and recyclable photocatalyst for photo-oxidation of *N*-alkylquinolinium iodide. We also demonstrated gram-scale synthesis of 1-methyl-5-nitroisoquinolinone using $Pt_{0.9}@PCN-221$ photocatalyst under visible-light irradiation (Table 1). A catalytic activity of $175.8 \text{ g} \cdot \text{g}_{\text{cat}}^{-1}$ was achieved within 6 h toward 1-methyl-5-nitroisoquinolinone, over 22 times higher than that of PCN-221 ($7.8 \text{ g} \cdot \text{g}_{\text{cat}}^{-1}$). As the reaction prolonged to 14 h, the yield of 1-methyl-5-nitroisoquinolinone reached 86.3%, over 16 times higher than that of PCN-221 (5.3%). Furthermore, we performed the recycle experiments in gram-scale reaction with 5 mg catalyst. As shown in Figure S33B, the yield of 1-methyl-5-nitroisoquinolinone remained over 90% after being reused three times, highlighting the excellent stability of $Pt_{0.9}@PCN-221$ for photosynthesis. The excellent photocatalytic stability of $Pt_{0.9}@PCN-221$ could be attributed to the encapsulation of Pt NCs into the cages of PCN-221, which can be used to well isolate Pt NCs to prevent the aggregation of entrapped NCs in the photocatalytic process.

Photocatalytic Mechanism

The mechanism of photo-oxidation by $Pt_{0.9}@PCN-221$ was studied in detail using 1a as substrate (Figures 4 and S34–S38). As shown in Figure 4A, the electron spin resonance (ESR) signals of PCN-221 detected *in situ* showed a light-dark difference that is consistent with the generation of porphyrin π -cation radical (Xu et al., 2018). $Pt_{0.9}@PCN-221$ showed similar ESR signals as PCN-221 but with a much larger light-dark difference (Figure 4A), suggesting much enhanced production of porphyrin π -cation radical in $Pt_{0.9}@PCN-221$ over PCN-221 due to electron transfer from photoexcited porphyrin to Pt NCs. To confirm this proposal, triethanolamine (TEOA), as a hole scavenger, was intentionally added to the photocatalytic reaction to quench porphyrin π -cation radicals (Xu et al., 2015; Yuan et al., 2017). As shown in Figure S35, the yield of 2a drastically decreased from 92.8% to 13.5% when the TEOA concentration increased from 0 M to 1.8 M. This result further indicates the important role of photogenerated holes in reacting with intermediates to facilitate complex catalytic reactions.

The increased yield of 2a in the O_2 atmosphere suggests that the oxidative species comes from O_2 . To ascertain the key oxidant in photocatalytic process, 4-oxo-2,2,6,6-tetramethyl-4-piperidone (4-oxo-TMP) and 5,5-dimethyl-1-pyrroline-*N*-oxide (DMPO) were employed to identify the production of 1O_2 and other reactive oxygen species (Figures 4, S37, and S38) (Konaka et al., 1999). In the presence of 4-oxo-TMP with

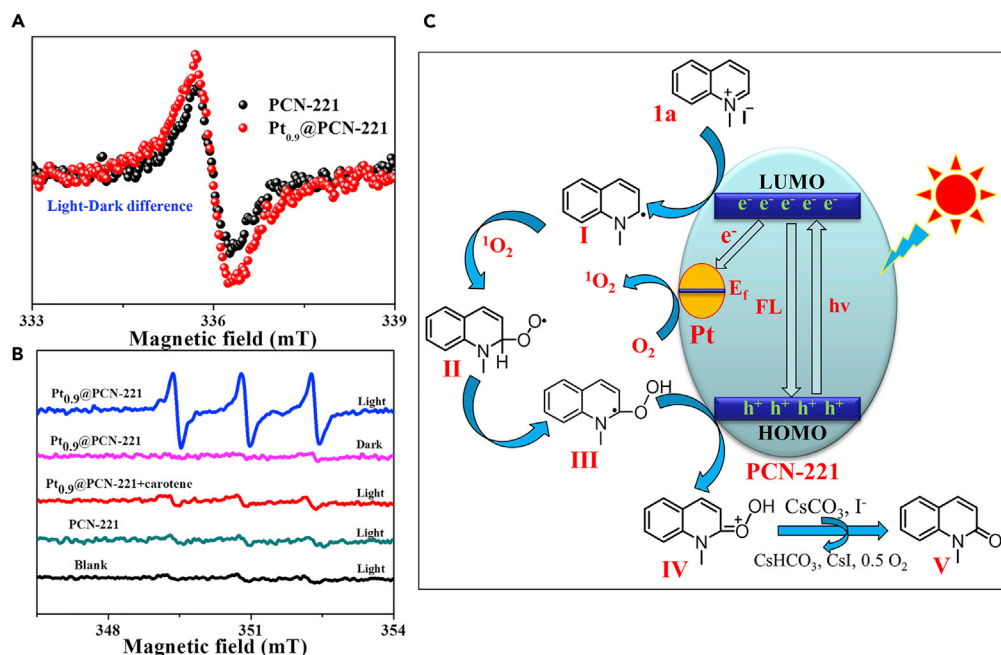


Figure 4. Photocatalytic Mechanism

(A) ESR detection of porphyrin π -cation radical in PCN-221 and Pt_{0.9}@PCN-221.

(B) ESR spectra of the solution containing 4-oxo-TMP and PCN-221/Pt_{0.9}@PCN-221 with/without carotene under visible-light irradiation or in dark.

(C) Proposed mechanism for visible-light-driven photo-oxidation of *N*-methylquinolinium iodide. E_f stands for the Fermi level of Pt NC; FL is the fluorescence.

Pt_{0.9}@PCN-221 as the catalyst, the ESR spectra display a 1:1:1 triplet signal that is consistent with the generation of ¹O₂ (Figure 4B) (Zhou et al., 2012). This triplet signal was almost completely quenched by carotene, a well-known scavenger for ¹O₂ via triplet-triplet energy transfer mechanism, confirming that the ESR signal originates from ¹O₂ (Badwey and Karnovsky, 1980). This ESR signal was absent under dark condition, indicating that light was a prerequisite for ¹O₂ generation. In comparison, PCN-221 just showed a weak ESR signal for ¹O₂ generation due to its poor ability to produce ¹O₂.

The generation of ¹O₂ was supported by PL spectroscopy. As shown in Figure S36, all the samples exhibited an emission peak at 1,265 nm corresponding to characteristic emission of ¹O₂ and the emission intensity decreased in the order of Pt_{0.9}@PCN-221 > Pt_{1.6}@PCN-221 > Pt_{3.0}@PCN-221 > PCN-221, which correlates with their photocatalytic activity (Table 1) (Wang et al., 2015). Notably, the signal of ¹O₂ significantly decreased after the addition of 1a to the above solution, suggesting the consumption of ¹O₂ by the substrate (Figure S37A). Furthermore, the yield of 2a significantly decreased from 92.8% to 28.9% with the addition of carotene, supporting the role of ¹O₂ as the oxidant in the photo-oxidation process (Figure S37B). In addition, the potential generation of O₂^{•-} and \cdot OH by Pt_{0.9}@PCN-221 was ruled out as no ESR signal was observed upon light irradiation when DMPO was used as a radical-trapping agent (Figure S38). These results thus demonstrate that ¹O₂ is efficiently generated in the Pt_{0.9}@PCN-221 photocatalytic system and acts as a predominant oxidant to promote the photo-oxidation reaction (Ogilby, 2010; Montagnon et al., 2008).

Finally, an intermediate radical in the photocatalytic reaction was detected by introducing DMPO into the mixture of Pt_{0.9}@PCN-221 and Cs₂CO₃ in the presence of substrate 1a. As shown in Figure S38, a sextet signal was generated upon excitation at 425 nm, which can be assigned to an alkylidioxyl DMPO radical adduct (Jin et al., 2017; Qian et al., 2017). Thus, this alkylidioxyl radical is proposed as intermediate II in this photocatalytic system (Figure 4C).

On the basis of the above-mentioned results, we propose the photocatalytic mechanism for Pt_{0.9}@PCN-221 as shown in Figure 4C. Upon excitation with visible light, electron-hole separation occurs on the porphyrin

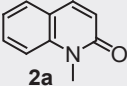
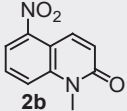
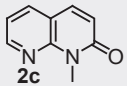
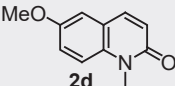
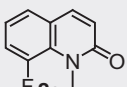
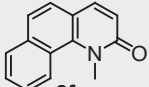
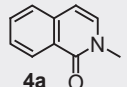
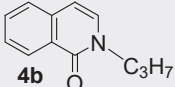
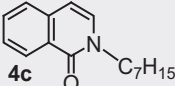
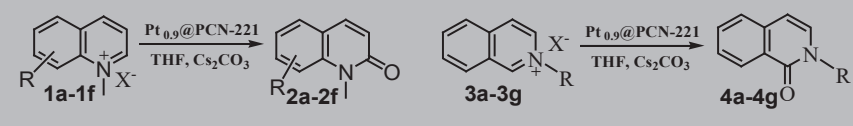
Entry	Product	t/h ^a	Yield/% ^b
1		2	92.8
2		1.5	93.4
3		2	91.6
4		3	80.6
5		2	88.3
6		2.5	69.5
7		2	95.3
8		1.5	91.2
9		1.5	94.7

Table 2. Visible Light-Driven Photo-oxidation of N-alkyl(iso)quinolinium Salts

(Continued on next page)



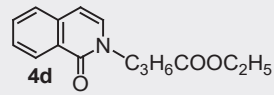
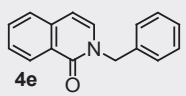
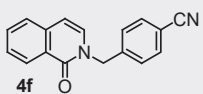
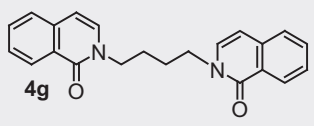
Entry	Product	t/h ^a	Yield/% ^b
10		2	81.2
11		2	86.2
12		2	82.1
13		3	90.5

Table 2. Continued

Reaction conditions: 1a–1f or 3a–3g (0.4 mmol); Pt_{0.9}@PCN-221 (0.068 mol%); Cs₂CO₃ (0.6 mmol); THF (4 mL); the mixture was irradiated with 425-nm LED in the air at room temperature.

^aReaction time.

^bYield of isolated products. X = I for 1a–f, 3a, 3c, and 3g; X = Br for 3b, 3d, and 3e.

ligand. The electron is quickly transferred to Pt NCs to promote ¹O₂ generation with the subsequent single electron transfer (SET) to 1a to afford radical I, which is further oxidized by ¹O₂ to afford alkylidioxyl radical intermediate II. Intermediate II is transformed into intermediate III via a hydrogen rearrangement process. The porphyrin π-cation has strong oxidation capacity to receive an electron from III via another SET process to produce cationic intermediate IV. IV can be easily transformed into the final product V by reacting with Cs₂CO₃ and I[−]. The Pt NC and PCN-221 framework thus synergistically promote electron-hole separation and ¹O₂ generation to greatly boost photo-oxidation of N-alkyl(iso)quinolinium salts to biologically active (iso)quinolinones.

Substrate Scope

Encouraged by the high activity of Pt_{0.9}@PCN-221 in photocatalytic oxidation of 1a, we examined the substrate scope with various N-methylquinolinium and N-alkylisoquinolinium salts (Table 2). Most of these reactions were highly efficient with the isolation of target products in >80.0% yields within 3 h. The substrates with electron-donating groups appear to exhibit a lower reactivity than those with electron-withdrawing groups. For example, relatively electron-rich substrate 2f with a large size shows a moderate reactivity to produce the corresponding quinolinone in 69.5% yields (Wu et al., 2012; Saito et al., 2013). The broad substrate scope and good functional group tolerance indicate that Pt_{0.9}@PCN-221 is indeed a state-of-the-art and robust catalyst with a unique mechanism for the photocatalytic oxidation of N-alkyl(iso)quinolinium salts.

DISCUSSION

In this work, we encapsulated ultrafine Pt NCs into PCN-221 by *in situ* photoreduction of K₂PtCl₄ to afford a family of heterogeneous photocatalysts Pt_x@PCN-221 (where x = 0.9, 1.6, 2.2, and 3.0 nm) with prominent Pt NC size-dependent catalytic activities in photo-oxidation of N-alkyl(iso)quinolinium salts. Synergistic

combination of photoexcited electron-hole separation with $^1\text{O}_2$ generation in $\text{Pt}_x\text{@PCN-221}$ greatly contributes to the excellent performance in (iso)quinolone synthesis from *N*-alkyl(iso)quinolinium salts. Among these composites, $\text{Pt}_{0.9}\text{@PCN-221}$ with sub-nm Pt NCs exhibits the best synergy of electron-hole separation and $^1\text{O}_2$ generation, leading to the highest activity of *N*-alkyl(iso)quinolinium photo-oxidation to produce (iso)quinolones in >90% yields. The heterogeneous photocatalyst was readily reused 10 times without a loss of catalytic activity. Thus, the photo-oxidation reaction can be easily extended to gram-scale synthesis of 1-methyl-5-nitrosoquinolinone at a catalytic activity of $175.8 \text{ g}\cdot\text{g}_{\text{cat}}^{-1}$, 22 times higher than that of PCN-221. Spectroscopic evidences and quenching results support the role of synergistic electron-hole separation and $^1\text{O}_2$ generation in photocatalytic *N*-alkyl (iso)quinolinium oxidation by the $\text{Pt}_x\text{@MOF}$ composite. This work thus presents a new strategy to integrate multiple functional components into MOF-based composite materials to synergistically catalyze complex photoreactions for the synthesis of biologically active heterocyclic molecules.

Limitations of the Study

In this article, we use sub-nm Pt nanocluster@MOFs as photocatalyst for efficient preparation of (iso)quinolones. However, the photocatalytic reaction was performed in THF, which is against the concept of green chemistry. In future work, the green solvent will be investigated.

METHODS

All methods can be found in the accompanying [Transparent Methods supplemental file](#).

SUPPLEMENTAL INFORMATION

Supplemental Information can be found online at <https://doi.org/10.1016/j.isci.2019.100793>.

ACKNOWLEDGMENTS

This work was supported by National Key R&D Program of China (2017YFA0700104) and the National Natural Science Foundation of China (No. 21722104, 21671032, 21703155), Natural Science Foundation of Tianjin City of China (18JCQNJC76500, 18JCQJJC47700, 17JCQNJC05100), and 111 Project of China (No. D17003).

AUTHOR CONTRIBUTIONS

S.G. and Z.-M.Z. conceived and designed this project; S.-S.F. and X.-Y.R. performed the experiments; S.-S.F., S.G., and Z.-M.Z. analyzed the data; S.-S.F., S.G., G.L., Z.-M.Z., T.-B.L., and W.L. wrote and revised the article.

DECLARATION OF INTERESTS

The authors declare no competing interests.

Received: October 9, 2019

Revised: December 10, 2019

Accepted: December 18, 2019

Published: January 24, 2020

REFERENCES

- Abdel-Mageed, A.-M., Rungtaweeworanit, B., Parlinska-Wojtan, M., Pei, X.-K., Yaghi, O.-M., and Behm, R.-J. (2019). Highly active and stable single-atom Cu catalysts supported by a metal-organic framework. *J. Am. Chem. Soc.* *141*, 5201–5210.
- Aijaz, A., and Xu, Q. (2014). Catalysis with metal nanoparticles immobilized within the pores of metal-organic frameworks. *J. Phys. Chem. Lett.* *5*, 1400–1411.
- Badwey, J.-A., and Karnovsky, M.-L. (1980). Active oxygen species and the functions of phagocytic leukocytes. *Ann. Rev. Biochem.* *49*, 695–726.
- Bai, Y., Dou, Y.-B., Xie, L.-H., Rutledge, W., Li, J.-R., and Zhou, H.-C. (2016a). Zr-based metal-organic frameworks: design, synthesis, structure, and applications. *Chem. Soc. Rev.* *45*, 2327–2367.
- Bai, L.-C., Wang, X., Chen, Q., Ye, Y.-F., Zheng, H.-Q., Guo, J.-H., Yin, Y.-D., and Gao, C.-B. (2016b). Explaining the size dependence in platinum-nanoparticle-catalyzed hydrogenation reactions. *Angew. Chem. Int. Ed.* *55*, 15656–15661.
- Cao, X.-H., Tan, C.-L., Sindoro, M., and Zhang, H. (2017). Hybrid micro-/nano-structures derived from metal-organic frameworks: preparation and applications in energy storage and conversion. *Chem. Soc. Rev.* *46*, 2660–2677.
- Carey, J.-S., Laffan, D., Thomson, C., and Williams, M.-T. (2006). Analysis of the reactions used for the preparation of drug candidate molecules. *Org. Biomol. Chem.* *4*, 2337–2347.
- Chen, Y.-Z., Wang, Z.-U., Wang, H.-H., Lu, J.-L., Yu, S.-H., and Jiang, H.-L. (2017). Singlet oxygen-engaged selective photo-oxidation over Pt nanocrystals/porphyrinic MOF: the roles of photothermal effect and Pt electronic state. *J. Am. Chem. Soc.* *139*, 2035–2044.

- Chen, F.-F., Shen, K., Chen, J.-Y., Yang, X.-F., Cui, J., and Li, Y.-W. (2019). General immobilization of ultrafine alloyed nanoparticles within metal-organic frameworks with high loadings for advanced synergetic catalysis. *ACS Cent. Sci.* **5**, 176–185.
- Choi, K.-M., Kim, D., Rungtaweeworant, B., Trickett, C.-A., Barmank, J.-T., Alshammari, A.-S., Yang, P., and Yaghi, O.-M. (2017). Plasmon-enhanced photocatalytic CO₂ conversion within metal-organic frameworks under visible light. *J. Am. Chem. Soc.* **139**, 356–362.
- Claassen, G., Brin, E., Crogan-Grund, C., Vaillancourt, M.-T., Zhang, H.-Z., Cai, S.-X., Drewe, J., Tseng, B., and Kasibhatla, S. (2009). Selective activation of apoptosis by a novel set of 4-aryl-3-(3-aryl-1-oxo-2-propenyl)-2(1H)-quinolinones through a myc-dependent pathway. *Cancer Lett.* **274**, 243–249.
- Deng, X., Li, Z., and Garcia, H. (2017). Visible light induced organic transformations using metal-organic-frameworks (MOFs). *Chem. Eur. J.* **23**, 11189–11209.
- Dhakshinamoorthy, A., Li, Z.-H., and Garcia, H. (2018). Catalysis and photocatalysis by metal organic frameworks. *Chem. Soc. Rev.* **47**, 8134–8172.
- Fan-Chiang, T.-T., Wang, H.-K., and Hsieh, J.-C. (2016). Synthesis of phenanthridine skeletal amaryllidaceae alkaloids. *Tetrahedron* **72**, 5640–5645.
- Forbis, R.-M., and Rinehart, K.-L. (1973). Nybomycin. VII. preparative routes to nybomycin and deoxynybomycin. *J. Am. Chem. Soc.* **95**, 5003–5013.
- Glushkov, V.-A., and Shklyayev, Y.-V. (2001). Synthesis of 1(2H)-isoquinolones. *Chem. Heterocycl. Compd.* **37**, 663–664.
- Howarth, A.-J., Liu, Y.-Y., Li, P., Li, Z.-Y., Wang, T.-C., Hupp, J.-T., and Farha, O.-K. (2016). Chemical, thermal and mechanical stabilities of metal-organic frameworks. *Nat. Rev. Mater.* **1**, 15018.
- Ishi-i, T., Hirashima, R., Tsutsumi, N., Amemori, S., Matsuki, S., Teshima, Y., Kuwahara, R., and Mataka, S. (2010). Expanded π -electron systems, tri(phenanthro)hexaazatriphenylenes and tri(phenanthro)hexaazatriphenylenes, that are self-assembled to form one-dimensional aggregates. *J. Org. Chem.* **75**, 6858–6868.
- Ji, P.-F., Manna, K., Lin, Z.-K., Feng, X.-Y., Urban, A., Song, Y., and Lin, W.-B. (2017). Single-site cobalt catalysts at new Zr₁₂(μ_3 -O)₈(μ_3 -OH)₈(μ_2 -OH)₆ metal-organic framework nodes for highly active hydrogenation of nitroarenes, nitriles, and isocyanides. *J. Am. Chem. Soc.* **139**, 7004–7011.
- Jin, Y.-H., Ou, L.-Y., Yang, H.-J., and Fu, H. (2017). Visible-light-mediated aerobic oxidation of N-alkylpyridinium salts under organic photocatalysis. *J. Am. Chem. Soc.* **139**, 14237–14243.
- Kandiah, M., Nilsen, M.H., Usseglio, S., Jakobsen, S., Olsbye, U., Tilset, M., Larabi, C., Quadrelli, E.A., Bonino, F., and Lillerud, K.P. (2010). Synthesis and stability of tagged UiO-66 Zr-MOFs. *Chem. Mater.* **22**, 6632–6640.
- Khalil, I.-M., Barker, D., and Copp, B.-R. (2016). Bioinspired syntheses of the pyridoadridine marine alkaloids demethyldeoxyamphimedine, deoxyamphimedine, and amphimedine. *J. Org. Chem.* **81**, 282–289.
- Konaka, R., Kasahara, E., Dunlap, W.C., Yamamoto, Y., Chien, K.C., and Inoue, M. (1999). Irradiation of titanium dioxide generates both singlet oxygen and superoxide anion. *Free Radic. Bio. Med.* **27**, 294–300.
- Kong, Z.-C., Liao, J.-F., Dong, Y.-J., Xu, Y.-F., Chen, H.-Y., Kuang, D.-B., and Su, C.-Y. (2018). Core@shell CsPbBr₃@zeolitic imidazolate framework nanocomposite for efficient photocatalytic CO₂ reduction. *ACS Energy Lett.* **3**, 2656–2662.
- Lee, J., Farha, O.-K., Roberts, J., Scheidt, K.-A., Nguyen, S.-T., and Hupp, J.-T. (2009). Metal-organic framework materials as catalysts. *Chem. Soc. Rev.* **38**, 1450–1459.
- Liu, J.-W., Chen, L.-F., Cui, H., Zhang, J.-Y., Zhang, L., and Su, C.-Y. (2014). Applications of metal-organic frameworks in heterogeneous supramolecular catalysis. *Chem. Soc. Rev.* **43**, 6011–6061.
- Liu, H., Xu, C.-Y., Li, D.-D., and Jiang, H.-L. (2018). Photocatalytic hydrogen production coupled with selective benzylamine oxidation over MOF composites. *Angew. Chem. Int. Ed.* **57**, 5379–5383.
- Liu, J., Shi, W., Ni, B., Yang, Y., Li, S., Zhuang, J., and Wang, X. (2019). Incorporation of clusters within inorganic materials through their addition during nucleation steps. *Nat. Chem.* **11**, 839–845.
- Luo, W.-K., Shi, X., Zhou, W., and Yang, L. (2016). Iodine-catalyzed oxidative functionalization of azarenes with benzylic C(Sp³)-H bonds via N-alkylation/amidation cascade: two-step synthesis of isoindolo[2,1-b]isoquinolin-7(5H)-one. *Org. Lett.* **18**, 2036–2039.
- Luo, Y.-H., Dong, L.-Z., Liu, J., Li, S.-L., and Lan, Y.-Q. (2019). From molecular metal complex to metal-organic framework: the CO₂ reduction photocatalysts with clear and tunable structure. *Coord. Chem. Rev.* **390**, 86–126.
- Montagnon, T., Tofi, M., and Vassilikogiannakis, G. (2008). Using singlet oxygen to synthesize polyoxygenated natural products from furans. *Acc. Chem. Res.* **41**, 1001–1011.
- Muzzio, M., Li, J., Yin, Z., Delahunty, I.-M., Xie, J., and Sun, S. (2019). Monodisperse nanoparticles for catalysis and nanomedicine. *Nanoscale* **11**, 18946–18967.
- Ni, Z.-J., Barsanti, P., Brammeier, N., Diebes, A., Poon, D.-J., Ng, S., Pecchi, S., Pfister, K., Renhowe, P.-A., Ramurthy, S., et al. (2006). 4-(Aminoalkylamino)-3-benzimidazole-quinolinones as potent CHK-1 inhibitors. *Bioorg. Med. Chem. Lett.* **16**, 3121–3124.
- Ogilby, P.-R. (2010). Singlet oxygen: there is indeed something new under the Sun. *Chem. Soc. Rev.* **39**, 3181–3209.
- Paille, G., Gomez-Mingot, M., Roch-Marchal, C., Lassalle-Kaiser, B., Mialane, P., Fontecave, M., Mellot-Draznics, C., and Dolbecq, A. (2018). A fully noble metal-free photosystem based on cobalt-polyoxometalates immobilized in a porphyrinic metal-organic framework for water oxidation. *J. Am. Chem. Soc.* **140**, 3613–3618.
- Pascanu, V., Gonzalez Miera, G., Inge, A.-K., and Martin-Matute, B. (2019). Metal-organic frameworks as catalysts for organic synthesis: a critical Perspective. *J. Am. Chem. Soc.* **141**, 7223–7234.
- Pullen, S., Fei, H., Orthaber, A., Cohen, S.M., and Ott, S. (2013). Enhanced photochemical hydrogen production by a molecular diiron catalyst incorporated into a metal-organic framework. *J. Am. Chem. Soc.* **135**, 16997–17003.
- Qian, P., Su, J.-H., Wang, Y.-K., Bi, M.-X., Zha, Z.-G., and Wang, Z.-Y. (2017). Electrocatalytic C-H/N-H coupling of 2'-aminoacetophenones for the synthesis of isatins. *J. Org. Chem.* **82**, 6434–6440.
- Saha, S., Das, G., Thote, J., and Banerjee, R. (2014). Photocatalytic metal-organic framework from CdS quantum dot incubated luminescent metallohydrogel. *J. Am. Chem. Soc.* **136**, 14845–14851.
- Saito, M., Toyao, T., Ueda, K., Kamegawa, T., Horiuchi, Y., and Matsuoka, M. (2013). Effect of pore sizes on catalytic activities of arenetricarbonyl metal complexes constructed within Zr-based MOFs. *Dalton Trans.* **42**, 9444–9447.
- Sarina, S., Zhu, H.-Y., Xiao, Q., Jaatinen, E., Jia, J.-F., Huang, Y.-M., Zheng, Z.-F., and Wu, H.-S. (2014). Visible photocatalysts under solar-spectrum irradiation: nonplasmonic metal nanoparticles. *Angew. Chem. Int. Ed.* **53**, 2935–2940.
- Sun, D., and Li, Z. (2016). Double-solvent method to Pd nanoclusters encapsulated inside the cavity of NH₂-UiO-66(Zr) for efficient visible-light-promoted Suzuki coupling reaction. *J. Phys. Chem. C* **120**, 19744–19750.
- Sun, D.-R., Xu, M.-P., Jiang, Y.-T., Long, J.-L., and Li, Z.-H. (2018). Small-sized bimetallic cupd nanoclusters encapsulated inside cavity of NH₂-UiO-66(Zr) with superior performance for light-induced Suzuki coupling reaction. *Small Methods* **2**, 1800164.
- Wang, D., and Li, Z. (2016). Coupling MOF-based photocatalysis with Pd catalysis over Pd@MIL-100 (Fe) for efficient N-alkylation of amines with alcohols under visible light. *J. Catal.* **342**, 151–157.
- Wang, C., deKrafft, K.-E., and Lin, W.-B. (2012). Pt nanoparticles@photoactive metal-organic frameworks: efficient hydrogen evolution via synergistic photoexcitation and electron injection. *J. Am. Chem. Soc.* **134**, 7211–7214.
- Wang, H.-L., Wang, Y.-H., Zhu, Z.-W., Sapi, A., An, K., Kennedy, G., Michalak, W.-D., and Somorjai, G.-A. (2013). Influence of size-induced oxidation state of platinum nanoparticles on selectivity and activity in catalytic methanol oxidation in the gas phase. *Nano Lett.* **13**, 2976–2979.
- Wang, H., Yang, X.-Z., Shao, W., Chen, S.-C., Xie, J.-F., Zhang, X.-D., Wang, J., and Xie, Y. (2015). Ultrathin black phosphorus nanosheets for efficient singlet oxygen generation. *J. Am. Chem. Soc.* **137**, 11376–11382.

Wang, D.-Y., Zhang, R.-X., Deng, R.-H., Lin, S., Guo, S.-M., and Yan, Z.-H. (2016). Copper-mediated oxidative functionalization of C(Sp³)-H bonds with isoquinolines: two-step synthesis of 5-oxaprotuberberinones. *J. Org. Chem.* *81*, 11162–11167.

Wu, C.-D., and Zhao, M. (2017). Incorporation of molecular catalysts in metal-organic frameworks for highly efficient heterogeneous catalysis. *Adv. Mater.* *29*, 1605446.

Wu, P.-Y., He, C., Wang, J., Peng, X.-J., Li, X.-Z., An, Y.-L., and Duan, C.-Y. (2012). Photoactive chiral metal-organic frameworks for light-driven asymmetric α -alkylation of aldehydes. *J. Am. Chem. Soc.* *134*, 14991–14999.

Wu, L.Y., Mu, Y.F., Guo, X.X., Zhang, W., Zhang, Z.-M., Zhang, M., and Lu, T.B. (2019). Encapsulating perovskite quantum dots in iron-based metal-organic frameworks (MOFs) for efficient photocatalytic CO₂ reduction. *Angew. Chem. Int. Ed.* *58*, 9491–9495.

Xia, Z.-Q., He, C., Wang, X.-G., and Duan, C.-Y. (2017). Modifying electron transfer between photoredox and organocatalytic units via framework interpenetration for β -carbonyl functionalization. *Nat. Commun.* *8*, 361.

Xiao, J.-D., and Jiang, H.-L. (2019). Metal-organic frameworks for photocatalysis and photothermal catalysis. *Acc. Chem. Res.* *52*, 356–366.

Xiao, J.-D., Shang, Q.-C., Xiong, Y.-J., Zhang, Q., Luo, Y., Yu, S.-H., and Jiang, H.-L. (2016). Boosting photocatalytic hydrogen production of a metal-organic framework decorated with platinum nanoparticles: the platinum location matters. *Angew. Chem. Int. Ed.* *128*, 9535–9539.

Xu, H.-Q., Hu, J.-H., Wang, D.-K., Li, Z.-H., Zhang, Q., Luo, Y., Yu, S.-H., and Jiang, H.-L. (2015). Visible-light photoreduction of CO₂ in a metal-organic framework: boosting electron-hole separation via electron trap states. *J. Am. Chem. Soc.* *137*, 13440–13443.

Xu, C.-Y., Liu, H., Li, D.-D., Su, J.-H., and Jiang, H.-L. (2018). Direct evidence of charge separation in a metal-organic framework: efficient and selective photocatalytic oxidative coupling of amines via charge and energy transfer. *Chem. Sci.* *9*, 3152–3158.

Yang, H., and Wang, X. (2018). Secondary-component incorporated hollow MOFs and derivatives for catalytic and energy-related applications. *Adv. Mater.* *31*, e1800743.

Yang, Q.-H., Xu, Q., and Jiang, H.-L. (2017). Metal-organic frameworks meet metal

nanoparticles: synergistic effect for enhanced catalysis. *Chem. Soc. Rev.* *46*, 4774–4808.

Yuan, Y.-J., Yu, Z.-T., Chen, D.-Q., and Zou, Z.-G. (2017). Metal-complex chromophores for solar hydrogen generation. *Chem. Soc. Rev.* *46*, 603–631.

Zhang, Z.-M., Zhang, T., Wang, C., Lin, Z.-K., Long, L.-S., and Lin, W.-B. (2015). Photosensitizing metal-organic framework enabling visible-light-driven proton reduction by a wells-dawson-type polyoxometalate. *J. Am. Chem. Soc.* *137*, 3197–3200.

Zhang, Y., Guo, J., Shi, L., Zhu, Y.-F., Hou, K., Zheng, Y.-L., and Tang, Z.-Y. (2017a). Tunable chiral metal organic frameworks toward visible light-driven asymmetric catalysis. *Sci. Adv.* *3*, e1701162.

Zhang, H., Nai, J., Yu, L., and Lou, X.W.(David) (2017b). Metal-organic-framework-based materials as platforms for renewable energy and environmental applications. *Joule* *1*, 77–107.

Zhou, H.-C., Long, J.-R., and Yaghi, O.-M. (2012). Introduction to metal-organic frameworks. *Chem. Rev.* *112*, 673–674.

iScience, Volume 23

Supplemental Information

Synergistic Effect over Sub-nm

Pt Nanocluster@MOFs Significantly Boosts

Photo-oxidation of *N*-alkyl(iso)quinolinium Salts

Shan-Shan Fu, Xiu-Ying Ren, Song Guo, Guangxu Lan, Zhi-Ming Zhang, Tong-Bu Lu, and Wenbin Lin

Supporting Information

Synergistic effect over sub-nm Pt nanocluster@MOFs significantly boosts photo-oxidation of N-alkyl(iso)quinolinium salts

Shan-Shan Fu,¹ Xiu-Ying Ren,² Song Guo,^{1*} Guangxu Lan,³ Zhi-Ming Zhang,^{1,2*} Tong-Bu Lu¹ and Wenbin Lin³

Table of Contents

- 1. Transparent Methods**
- 2. Supplementary Figures**
- 3. Supplementary Tables**

1. Transparent Methods

Materials: Potassium tetrachloroplatinate (K_2PtCl_4 , 98.0%), *N, N*-diethylformamide (DEF), zirconium chloride ($ZrCl_4$, 98.0%) were purchased from Sigma Aldrich. 2,2,6,6-tetramethyl-4-piperidone hydrochloride (4-oxo-TMP, 98.0%) was purchased from Adamas. Triethylamine (TEA, 99.0%) and triethanolamine (TEOA, > 99.0%) were received from Aladdin. All of the chemicals were obtained from commercial sources and used without further purification unless otherwise stated.

Characterization: Powder X-ray diffraction (PXRD) data were collected on a Smart X-ray diffractometer (SmartLab 9 KW, Rigaku, Japan) with Cu $K\alpha$ radiation ($\lambda = 1.54178 \text{ \AA}$). The morphologies of these samples were investigated by high-resolution scanning electron microscopy (HRSEM, Verios 460L) and high-resolution transmission electron microscope (HRTEM, Talos F200 X). The morphologies of these samples were investigated by high-resolution scanning electron microscopy (HRSEM, Verios 460L) and high-resolution transmission electron microscope (HRTEM, Talos F200 X). Energy dispersive X-ray spectroscopy (EDS) was recorded on a Tecnai G2 Energy Dispersive X-ray Spectrometer. The amounts of Pt loading in MOFs were determined by the inductively coupled plasma-atomic emission spectroscopy (ICP-AES, SPECTRO-BLUE). X-ray photoelectron spectra (XPS) were collected on an ESCALAB250Xi with Mg $K\alpha$ ($h\nu = 1253.6 \text{ eV}$) as the excitation source, using C 1s to 284.6 eV as reference. The electron spin resonance (ESR) measurements were performed with a Bruker Elexsys X-band (9.7 GHz) E580 EPR spectrometer. Brunauer-Emmett-Teller (BET) measurements were performed with N_2 adsorption-desorption isotherms at liquid nitrogen temperature (77 K) using automatic volumetric adsorption equipment (BELSORP-max). UV-vis absorption measurements were recorded using a LAMBDA750 UV-vis spectrophotometer. Fluorescence spectra were taken on a Hitachi F4500 spectrofluorimeter. Time-Correlated Single Photon Counting (TCSPC) measurements were performed by Micro Time 200 time-resolved confocal fluorescence instrument. Photocatalytic experiments were conducted with a 425 nm LED light (model: MLED4, brand: zolix, light intensity: 100 mW/cm^2). 1H NMR spectra were recorded on AVANCE III HD 400MHz Digital NMR Spectrometer (Bruker, German)

Synthesis of PCN-221. PCN-221 was synthesized according to the previous report (Feng, et al., 2018). The typical procedure is as follows: $ZrCl_4$ (7 mg), H_2TCPP (10 mg), and acetic acid (100 μL) were ultrasonically dissolved in 2 mL DEF in a Pyrex vial. The mixture was heated to 120 $^\circ\text{C}$ in an oven for 12 h. After cooling to room temperature, dark red powder was

obtained through filtration and washed with DEF. The powder was confirmed to be PCN-221 by PXRD analysis.

Preparation of Pt_x@PCN-221 (where x = 0.9, 1.6, 2.2 and 3.0 nm)

K₂PtCl₄ and PCN-221 powder were added in a mixed solvent of tetrahydrofuran (THF) / triethylamine (TEA) / H₂O (12/1/2 v/v/v). The suspension was degassed by bubbling with N₂ for 15 min and then placed in front of a 300 W Xe-lamp with a 420 nm cutoff (long pass) filter. Condition for Pt_{0.9}@PCN-221: K₂PtCl₄ (9.2 mg), PCN-221 (14.0 mg), 20 cycles of light (6 s) and darkness (54 s) for 20 min; for Pt_{1.6}@PCN-221: K₂PtCl₄ (9.2 mg), PCN-221 (14.0 mg), 60 cycles of light (6 s) and darkness (54 s) for 60 min; for Pt_{2.2}@PCN-221: K₂PtCl₄ (1.8 mg), PCN-221 (14.0 mg), 20 cycles of light (6 s) and darkness (54 s) for 20 min; for Pt_{3.0}@PCN-221: K₂PtCl₄ (18.3 mg), PCN-221 (14.0 mg), 60 cycles of light (6 s) and darkness (54 s) for 60 min.

Preparation of Pt_x@N-C (N-C stands for N-doping porous carbon)

Under Ar atmosphere, Pt_x@PCN-221 samples were calcined at 500 °C in a tube furnace for 4 hours. After cooling to room temperature, the products were washed with 5 wt% HF to remove ZrO₂ and then washed with ultrapure water. The black powder was obtained and denoted Pt_x@N-C, x = 0.9, 1.6, 2.2 and 3.0.

Typical procedures for photocatalytic organic reactions

N-methylpyridinium iodide and *N*-alkylisoquinoline salt (0.4 mmol), 2 mg photocatalysts (0.068 mol% Pt vs. 1a for Pt_{0.9}@PCN-221, 0.073 mol% Pt vs. 1a for Pt_{1.6}@PCN-221, 0.030 mol% Pt vs. 1a for Pt_{2.2}@PCN-221, 0.022 mol% Pt vs. 1a for Pt_{3.0}@PCN-221), Cs₂CO₃ (0.6 mmol), and THF (4 mL) were mixed in a 5 mL quartz tube. The mixture was irradiated with a 425 nm LED under air atmosphere at room temperature. After the substrates were converted completely (monitored by thin layer chromatography measurement (TLC)), the mixture was purified by silica gel column chromatography. To further test the reusability, the catalysts after the catalytic reactions were separated and collected by centrifugation, and then used for the next cycle without further activation. For gram-scale synthesis, 1-methyl-5-nitroisoquinolin iodide (1.0 g, 3.2 mmol), Pt_{0.9}@PCN-221 (0.0084 mol % Pt vs. 1b), Cs₂CO₃ (0.9 mmol) and THF (6 mL) were used in the photocatalytic reaction. The reaction was completed in 14 h as monitored by TLC. For gram-scale recycle experiment, 1-methyl-5-nitroisoquinolin iodide (1.0 g, 3.2 mmol), Pt_{0.9}@PCN-221 (5 mg, 0.022 mol% Pt vs. 1b), Cs₂CO₃ (293.4 mg, 0.9 mmol) and THF (6 mL) were mixed in a quartz tube. The reaction was monitored by TLC and completed in 6 h upon irradiation with visible light. After the catalytic reactions, the catalysts were separated and collected by centrifugation, and then used for next

cycle without further activation. All of the substrates and products were characterized by ^1H NMR (Figure S1-S26).

Photoelectrochemical measurements. A blue LED light (425 nm) was used as the light source. Na_2SO_4 aqueous solution (0.2 M) was used as the electrolyte. Working electrode was prepared as follows: as-synthesized samples (1 mg) were added to a solution containing 10 μL Nafion and 1 mL ethanol. The suspension (15 μL) was dropped onto the surface of an FTO plate (1 cm^2) to obtain the working electrode. Pt wire and Ag/AgCl were used as the counter electrode and reference electrode, respectively. The photoresponse signals of these samples were measured under chopped light at 0.6 V. The electrochemical impedance spectroscopy (EIS) was performed in the frequency range of 10^{-1} - 10^6 Hz with a bias potential of 2.0 V.

ESR detection of porphyrin cation radicals over PCN-221 and $\text{Pt}_x\text{@PCN-221}$. ESR measurements were carried out with PCN-221 and $\text{Pt}_x\text{@PCN-221}$ under irradiation with a 425 nm LED at 140 K under open air atmosphere in a quartz cube.

ESR detection of $^1\text{O}_2$ over PCN-221 and $\text{Pt}_x\text{@PCN-221}$. 10 μL of PCN-221/THF suspension or $\text{Pt}_x\text{@PCN-221}$ /THF suspension (5 mg mL^{-1}) was mixed with 500 μL of 4-oxo-TMP/THF suspension ($C_{4\text{-oxo-TMP}} = 150$ mM). The measurements were conducted at room temperature under irradiation with 425 nm LED or in the dark.

Synthesis and ^1H NMR spectra of substrates and products.

Synthesis of 1-methylquinoline iodide (1a). **1a** was synthesized according to the reported literature (Wu, et al., 2016). Quinoline (848.6 μL , 7.16 mmol) was first dispersed in dry toluene (50 mL). CH_3I (548.2 μL , 8.81 mmol) was then added to the above solution at room temperature. The resulting mixture was refluxed under argon for 1 h. After cooling to room temperature, the precipitate was collected and dried (1.8 g, 94.2 %). ^1H NMR (400 MHz, $\text{DMSO-}d_6$) δ 9.51 (d, $J = 5.6$ Hz, 1H), 9.29 (d, $J = 8.4$ Hz, 1H), 8.53 (d, $J = 8.9$ Hz, 1H), 8.49 (d, $J = 8.3$ Hz, 1H), 8.31 (t, $J = 7.9$ Hz, 1H), 8.17 (t, $J = 7.1$ Hz, 1H), 8.08 (t, $J = 7.6$ Hz, 1H), 4.65 (s, 3H).

Synthesis of 1-methyl-5-nitroisoquinoline iodide (1b). **1b** was synthesized according to the reported literature (Wang, et al., 2018). A mixture of 5-nitroquinoline (2.5 g, 14 mmol) and CH_3I (2.7 mL, 43 mmol) in 4 mL DMF was heated to 40 $^\circ\text{C}$. After 2 h of reaction, the mixture was cooled to room temperature and diluted with acetone. The solid was filtered, washed and dried to give **1b** as a crimson solid (3.8 g, 85.5 %). ^1H NMR (400 MHz, $\text{DMSO-}d_6$) δ 9.68 (d, $J = 5.6$ Hz, 1H), 9.53 (d, $J = 9.0$ Hz, 1H), 8.92 (d, $J = 8.9$ Hz, 1H), 8.78 (d, $J = 7.7$ Hz, 1H), 8.48 – 8.34 (m, 2H), 4.72 (s, 3H).

Synthesis of 1-methyl-1,8-naphthyridin iodide (1c). 1c was synthesized according to the reported literature (Wu, et al., 2016). The reaction procedure was similar to that of 1a, except replacing quinoline with 1,8-naphthyridine (933.8 mg, 7.16 mmol). A pale yellow solid of 1c was collected and dried (1.7 g, 85.5 %). $^1\text{H NMR}$ (400 MHz, $\text{DMSO-}d^6$) δ 9.73 (d, $J = 5.7$ Hz, 1H), 9.44 – 9.41 (m, 1H), 9.37 (d, $J = 8.3$ Hz, 1H), 9.02 – 8.95 (m, 1H), 8.27 – 8.30 (m, 1H), 8.14 – 8.17 (m, 1H), 4.62 (s, 3H).

Synthesis of 6-methoxy-1-methylquinoline iodide (1d). 1d was synthesized according to the reported literature (Wu, et al., 2016). The reaction procedure was similar to that of 1a, except replacing quinoline with 6-methoxyquinoline (993.2 μL , 7.16 mmol). A yellow solid of 1d was collected and dried (1.9 g, 88.1 %). $^1\text{H NMR}$ (400 MHz, $\text{DMSO-}d^6$) δ 9.31 (d, $J = 5.6$ Hz, 1H), 9.11 (d, $J = 8.5$ Hz, 1H), 8.44 (d, $J = 9.3$ Hz, 1H), 8.14 – 8.07 (m, 1H), 7.95 – 7.89 (m, 2H), 4.61 (s, 3H), 4.01 (s, 3H).

Synthesis of 8-fluoro-1-methylquinoline iodide (1e). 1e was synthesized according to the reported literature (Barfield, et al., 1982). 8-Fluoroquinoline (0.52 g, 3.5 mmol) and iodomethane (2.5 g, 17.5 mmol) were dissolved in benzene (10 mL). After refluxed for 2 h, the mixture was cooled to room temperature. The resulting solid was crystallized from ethanol to give yellow needles of 1e (0.9 g, 93.1 %). $^1\text{H NMR}$ (400 MHz, $\text{DMSO-}d^6$) δ 9.49 (d, $J = 5.6$ Hz, 1H), 9.32 (d, $J = 8.5$ Hz, 1H), 8.31 (d, $J = 8.1$ Hz, 1H), 8.26 – 8.11 (m, 2H), 8.04 – 8.01 (m, 1H), 4.76 (d, $J = 8.8$ Hz, 3H).

Synthesis of 1-methylbenzoquinoline iodide (1f). The reaction procedure for 1f was similar to that of 1a (Wu, et al., 2016), except replacing quinoline with 7, 8 –benzoquinoline (528 μL , 3.5 mmol). A pale yellow solid of 1f was collected and dried (0.89 g, 71.2 %). $^1\text{H NMR}$ (400 MHz, CDCl_3) δ 9.31 (d, $J = 7.9$ Hz, 1H), 9.13 – 8.95 (m, 1H), 8.28 – 8.15 (m, 1H), 7.92 (d, $J = 8.1$ Hz, 1H), 7.83 (d, $J = 8.8$ Hz, 1H), 7.79 – 7.66 (m, 3H), 7.60 – 7.50 (m, 1H), 4.47 (s, 3H).

Synthesis of 2-methylisoquinoline iodide (3a). The reaction procedure for 3a was similar to that of 1a (Wu, et al., 2016), except replacing quinoline with isoquinoline. An aqua solid of 3a was collected and dried (1.7 g, 87.6 %). $^1\text{H NMR}$ (400 MHz, $\text{DMSO-}d^6$) δ 9.99 (s, 1H), 8.69 (d, $J = 6.4$ Hz, 1H), 8.56 (d, $J = 6.3$ Hz, 2H), 8.34 (d, $J = 8.0$ Hz, 2H), 8.07 (t, $J = 7.0$ Hz, 1H), 4.47 (s, 3H).

Synthesis of 2-propylisoquinoline bromide (3b). 3b was synthesized according to the reported literature (He, et al., 2018). Isoquinoline (6.5 g, 0.05 mol) and 1-bromopropane (6.8 g, 0.055 mol) were dissolved in ethyl acetate (14 mL), and the mixture was vigorously stirred at 60 $^\circ\text{C}$ for 2 days. After cooling to room temperature, the mixture was extracted with ethyl acetate. A pale yellow solid of 3b was collected and dried (11.8 g, 85.4 %). $^1\text{H NMR}$ (400

MHz, DMSO- d^6) δ 10.08 (s, 1H), 8.80 (d, $J = 5.8$ Hz, 1H), 8.60 (d, $J = 6.2$ Hz, 1H), 8.48 (d, $J = 7.8$ Hz, 1H), 8.37 – 8.27 (m, 2H), 8.09 (d, $J = 7.2$ Hz, 1H), 4.68 (s, 2H), 2.05 (d, $J = 7.1$ Hz, 2H), 0.93 (t, $J = 7.2$ Hz, 3H).

Synthesis of 2-heptylisoquinoline iodide (3c). The reaction procedure for 3c was similar to that of 3b (He, et al., 2018), except replacing 1-bromopropane with 1-iodoheptane. A purple solid of 3c was collected and dried (16.3 g, 86.3 %). ^1H NMR (400 MHz, DMSO- d^6) δ 10.09 (s, 1H), 8.81 (d, $J = 6.8$, 1H), 8.60 (d, $J = 6.8$, 1H), 8.49 (d, $J = 8.3$, 1H), 8.40 – 8.22 (m, 2H), 8.09 (t, $J = 7.6$, 1H), 4.71 (t, $J = 7.4$, 2H), 2.02– 1.99 (m, 2H), 1.48 – 1.11 (m, 9H), 0.85 (t, $J = 6.8$, 3H).

Synthesis of 2-(4-ethoxy-4-oxobutyl) isoquinolinebromine (3d). The reaction procedure for 3d was similar to that of 1a (Wu, et al., 2016), except replacing CH_3I and quinoline with ethyl 4-bromobutyrate and isoquinoline. A pale yellow oily product of 3d was collected and dried (2.1 g, 86.5 %). ^1H NMR (400 MHz, DMSO- d^6) δ 10.21 (s, 1H), 8.86 (d, $J = 6.8$, 1H), 8.64 (d, $J = 6.8$, 1H), 8.52 (d, $J = 8.3$, 1H), 8.38 (d, $J = 8.2$, 1H), 8.33 – 8.23 (m, 1H), 8.09 (t, $J = 7.6$, 1H), 4.81 (t, $J = 7.1$, 2H), 4.01 – 3.96 (m, 2H), 2.58 – 2.41 (m, 3H), 2.40 – 2.23 (m, 2H), 1.13 (t, $J = 7.1$, 3H).

Synthesis of 2-benzylisoquinoline bromide (3e). The reaction procedure for 3e was similar to that of 1a (Wu, et al., 2016), except replacing CH_3I / quinoline with benzylbromide / isoquinoline. A pale yellow solid of 3e was collected and dried (2.5 g, 87.6 %). ^1H NMR (400 MHz, DMSO- d^6) δ 10.29 (s, 1H), 8.83 (d, $J = 6.8$ Hz, 1H), 8.68 – 8.47 (m, 2H), 8.43 – 8.22 (m, 2H), 8.09 (t, $J = 7.6$ Hz, 1H), 7.59 (d, $J = 6.4$ Hz, 2H), 7.51 – 7.37 (m, 3H), 5.98 (s, 2H).

Synthesis of 4-benzonitrileisoquinoline bromide (3f). The reaction procedure for 3f was similar to that of 1a (Wu, et al., 2016), except replacing CH_3I / quinoline with 4-bromobenzonitrile / isoquinoline. A white solid of 3f was obtained (2.1 g, 91.2 %). ^1H NMR (400 MHz, DMSO- d^6) δ 10.24 (s, 1H), 8.80 (d, $J = 5.7$ Hz, 1H), 8.66 – 8.48 (m, 2H), 8.41 – 8.24 (m, 2H), 8.11 (d, $J = 7.0$ Hz, 1H), 7.94 (d, $J = 7.9$ Hz, 2H), 7.74 (d, $J = 7.9$ Hz, 2H), 6.07 (s, 2H).

Synthesis of butyl -1, 4-diisoquinoline iodide (3g). The reaction procedure for 3g was similar to that of 1a (Wu, et al., 2016), except replacing quinolone with butyl-1,4-diisoquinoline. A yellow solid of 3g was obtained (3.4 g, 83.6 %). ^1H NMR (400 MHz, DMSO- d^6) δ 10.08 (s, 2H), 8.78 (d, $J = 5.4$ Hz, 2H), 8.61 (d, $J = 6.2$ Hz, 2H), 8.47 (d, $J = 8.3$ Hz, 2H), 8.41 – 8.21 (m, 4H), 8.08 (t, $J = 7.0$ Hz, 2H), 4.79 (s, 4H), 2.12 (s, 4H).

Methylquinolin-2(1H)-one (2a). A pale yellow solid was obtained after purification by silica gel column chromatography (Eluent: PE/EtOAc = 1/1.25, v/v). Yield: 92.8 %. ^1H NMR (400

MHz, CDCl₃) δ 7.69 (d, J = 9.5 Hz, 1H), 7.58 (t, J = 7.8 Hz, 2H), 7.38 (d, J = 8.5 Hz, 1H), 7.24 (d, J = 7.7 Hz, 1H), 6.74 (d, J = 9.5 Hz, 1H), 3.74 (s, 3H).

Methyl-5-nitroquinolin-2(1H)-one (2b). An orange-red solid was obtained after purification by silica gel column chromatography (Eluent: PE/EtOAc = 1/1.5, v/v). Yield: 93.4 %. ¹H NMR (400 MHz, CDCl₃) δ 8.29 (d, J = 10.1 Hz, 1H), 7.88 – 7.78 (m, 1H), 7.73 – 7.61 (m, 2H), 6.91 (d, J = 10.1 Hz, 1H), 3.78 (s, 3H).

Methyl-1,8-naphthyridin-2(1H)-one (2c). A pale yellow solid was obtained by silica gel column chromatography (Eluent: PE/EtOAc = 1/1, v/v). Yield: 91.6 %. ¹H NMR (400 MHz, CDCl₃) δ 8.67 – 8.52 (m, 1H), 7.90 – 7.79 (m, 1H), 7.65 (d, J = 9.5 Hz, 1H), 7.22 – 7.11 (m, 1H), 6.77 (d, J = 9.5 Hz, 1H), 3.84 (s, 3H).

6-Methoxy-1-methylquinolin-2(1H)-one (2d). A pale yellow solid was obtained by silica gel column chromatography (Eluent: PE/EtOAc = 1/1.5, v/v). Yield: 80.6 %. ¹H NMR (400 MHz, CDCl₃) δ 7.61 (d, J = 9.5, 1H), 7.31 (d, J = 9.2, 1H), 7.22 – 7.16 (m, 1H), 7.01 (d, J = 2.8, 1H), 6.72 (d, J = 9.5, 1H), 3.87 (s, 3H), 3.71 (s, 3H).

8-Fluoro-1-methylquinolin-2(1H)-one (2e). A pale yellow solid was obtained after purification by silica gel column chromatography (Eluent: PE/EtOAc = 1.5/1, v/v). Yield: 88.3 %. ¹H NMR (400 MHz, DMSO-*d*⁶) δ 7.97 – 7.88 (m, 1H), 7.55 (d, J = 7.7, 1H), 7.52 – 7.43 (m, 1H), 7.30 – 7.19 (m, 1H), 6.67 (d, J = 9.5, 1H), 3.78 (d, J = 8.6, 3H).

Methylbenzo[*h*]quinolin-2(1H)-one (2f). A pale yellow solid was obtained after purification by silica gel column chromatography (Eluent: PE/EtOAc = 2.5/1, v/v). Yield: 69.5 %. ¹H NMR (400 MHz, CDCl₃) δ 8.46 (d, J = 8.9 Hz, 1H), 7.89 (d, J = 8.3 Hz, 1H), 7.75 (d, J = 8.9 Hz, 1H), 7.62 – 7.50 (m, 3H), 7.47 (d, J = 8.3 Hz, 1H), 6.80 (d, J = 8.9 Hz, 1H), 4.07 (s, 3H).

2-Methylisoquinolin-1(2H)-one (4a). A pale yellow oil was obtained after purification by silica gel column chromatography (Eluent: PE/EtOAc = 1:1, v/v). Yield: 95.3 %. ¹H NMR (400 MHz, CDCl₃) δ 8.43 (d, J = 7.6 Hz, 1H), 7.67 – 7.58 (m, 1H), 7.56 – 7.43 (m, 2H), 7.07 (d, J = 7.2 Hz, 1H), 6.48 (d, J = 7.1 Hz, 1H), 3.61 (s, 3H).

2-Propylisoquinolin-1(2H)-one (4b). A pale yellow oil was obtained after purification by silica gel column chromatography (Eluent: PE/EtOAc = 3/1, v/v). Yield: 91.2 %. ¹H NMR (400 MHz, CDCl₃) δ 8.44 (d, J = 7.7 Hz, 1H), 7.65 – 7.57 (m, 1H), 7.53 – 7.43 (m, 2H), 7.05 (d, J = 7.3 Hz, 1H), 6.48 (d, J = 7.2 Hz, 1H), 3.96 (t, J = 7.3 Hz, 2H), 1.87 – 1.75 (m, 2H), 0.98 (t, J = 7.4, 3H).

2-Heptylisoquinolin-1(2H)-one (4c). A pale yellow oil was obtained by silica gel column chromatography (Eluent: PE/EtOAc = 5:1, v/v). Yield: 94.7 %. ¹H NMR (CDCl₃, 400 MHz) δ 8.42 (d, J = 7.6 Hz, 1H), 7.59 (t, J = 7.6 Hz, 1H), 7.50 – 7.42 (m, 2H), 7.04 (d, J = 7.6 Hz,

1H), 6.46 (d, $J = 7.6$ Hz, 1H), 3.97 (t, $J = 7.6$ Hz, 2H), 1.78 – 1.73 (m, 2H), 1.39 – 1.16 (m, 8H), 0.86 (t, $J = 6.9$ Hz, 3H).

Ethyl 4-(1-oxoisoquinolin-2(1H)-yl)butanoate (4d). A pale yellow oil was obtained by silica gel column chromatography (Eluent: PE/EtOAc = 4:1, v/v). Yield: 81.2 %. ^1H NMR (CDCl_3 , 400 MHz) δ 8.41 (d, $J = 8.2$ Hz, 1H), 7.62 (t, $J = 7.6$ Hz, 1H), 7.53– 7.41 (m, 2H), 7.07 (d, $J = 7.6$ Hz, 1H), 6.49 (d, $J = 6.9$ Hz, 1H), 4.10 (q, $J = 6.9$ Hz, 2H), 4.04 (t, $J = 6.9$ Hz, 2H), 2.39 (t, $J = 7.2$ Hz, 2H), 2.10 (q, $J = 6.2$ Hz, 2H), 1.23 (t, $J = 7.2$ Hz, 3H).

2-Benzylisoquinolin-1(2H)-one (4e). A pale yellow solid was obtained by silica gel column chromatography (Eluent: PE/EtOAc = 5/1, v/v). Yield: 86.2 %. ^1H NMR (400 MHz, CDCl_3) δ 8.46 (d, $J = 7.6$ Hz, 1H), 7.66 – 7.58 (m, 1H), 7.49 (d, $J = 7.6$ Hz, 2H), 7.37 – 7.23 (m, 5H), 7.07 (d, $J = 7.3$ Hz, 1H), 6.47 (d, $J = 7.2$ Hz, 1H), 5.22 (s, 2H).

4-((1-Oxoisoquinolin-2(1H)-yl)methyl)benzotrile (4f). A pale yellow solid was obtained by silica gel column chromatography (Eluent: PE/EtOAc = 3/1, v/v). Yield: 82.1 %. ^1H NMR (400 MHz, CDCl_3) δ 8.44 (d, $J = 8.2$, 1H), 7.67 (t, $J = 7.6$, 1H), 7.63 (d, $J = 8.3$, 2H), 7.53 (d, $J = 8.1$, 2H), 7.41 (d, $J = 8.3$, 2H), 7.07 (d, $J = 7.4$, 1H), 6.55 (d, $J = 7.3$, 1H), 5.26 (s, 2H).

2,2'-(Butane-1,4-diyl)bis(isoquinolin-1(2H)-one) (4g). A white solid was obtained by silica gel column chromatography (Eluent: PE/EtOAc = 1/2, v/v). Yield: 90.5 %. ^1H NMR (400 MHz, CDCl_3) δ 8.42 (d, $J = 8.3$ Hz, 2H), 7.60 (t, $J = 7.0$ Hz, 2H), 7.50 – 7.32 (m, 4H), 7.06 (d, $J = 6.2$ Hz, 2H), 6.46 (d, $J = 6.2$ Hz, 2H), 4.10 – 3.92 (m, 4H), 1.90 – 1.70 (m, 4H).

2. Supplementary Figures

Supplementary figures for ^1H -NMR spectra of substrate 1a-1f and 3a-3g.

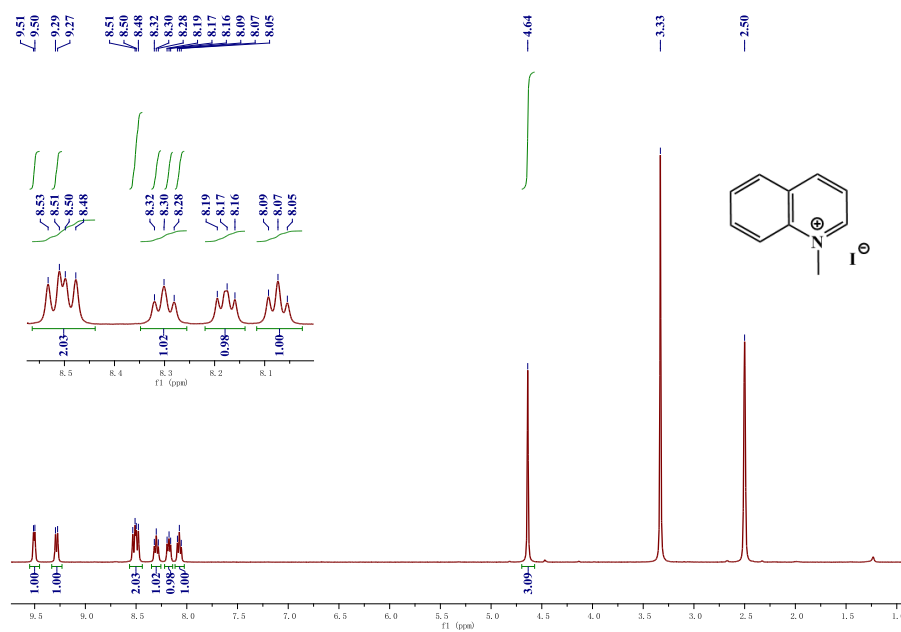


Figure S1. ^1H NMR of 1a in DMSO-d_6 (400 MHz), related to Table 1 and Table 2.

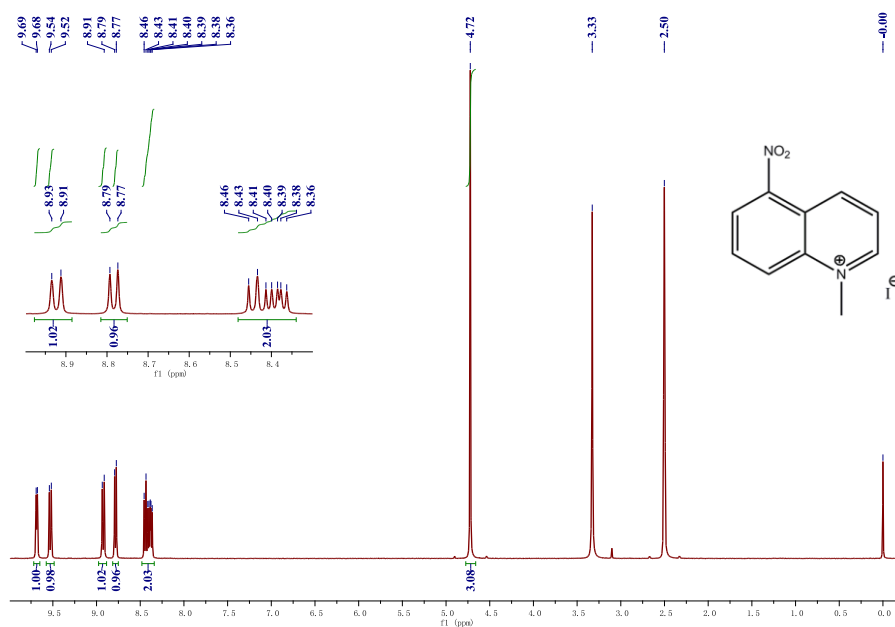


Figure S2. ^1H NMR of 1b in DMSO-d_6 (400 MHz), related to Table 2.

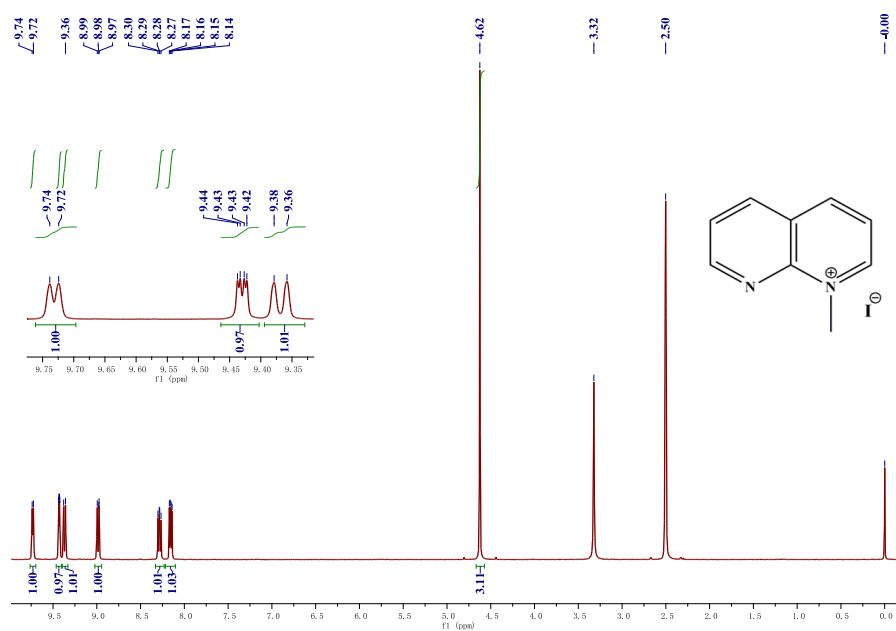


Figure S3. ^1H NMR of 1c in DMSO-d^6 (400 MHz), related to Table 2.

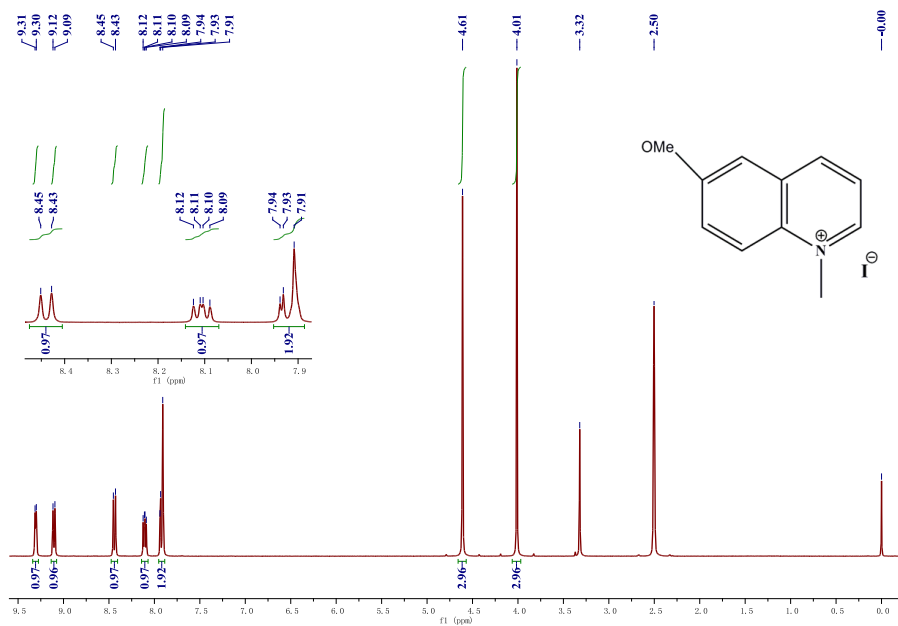


Figure S4. ^1H NMR of 1d in DMSO-d^6 (400 MHz), related to Table 2.

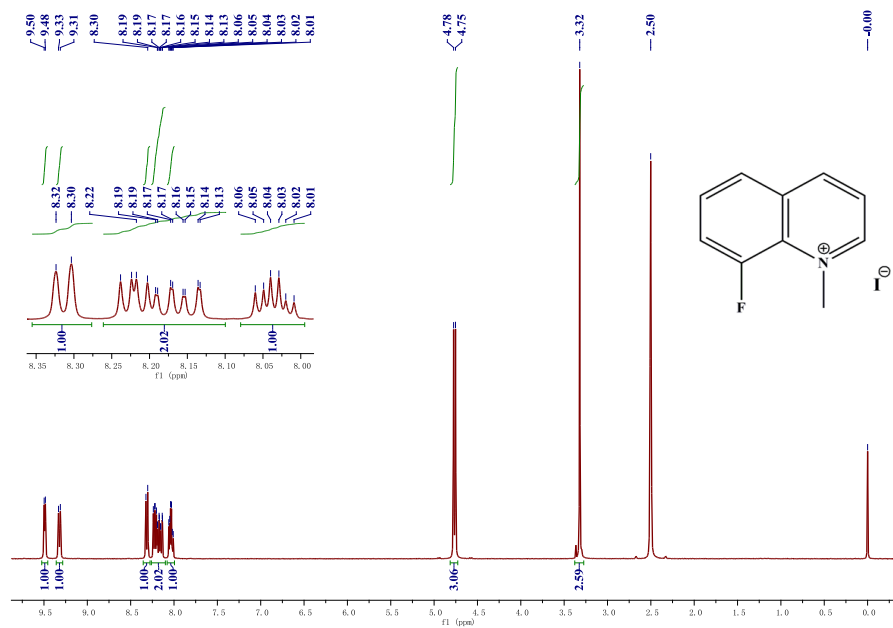


Figure S5. ^1H NMR of 1e in $\text{DMSO-}d_6$ (400 MHz), related to Table 2.

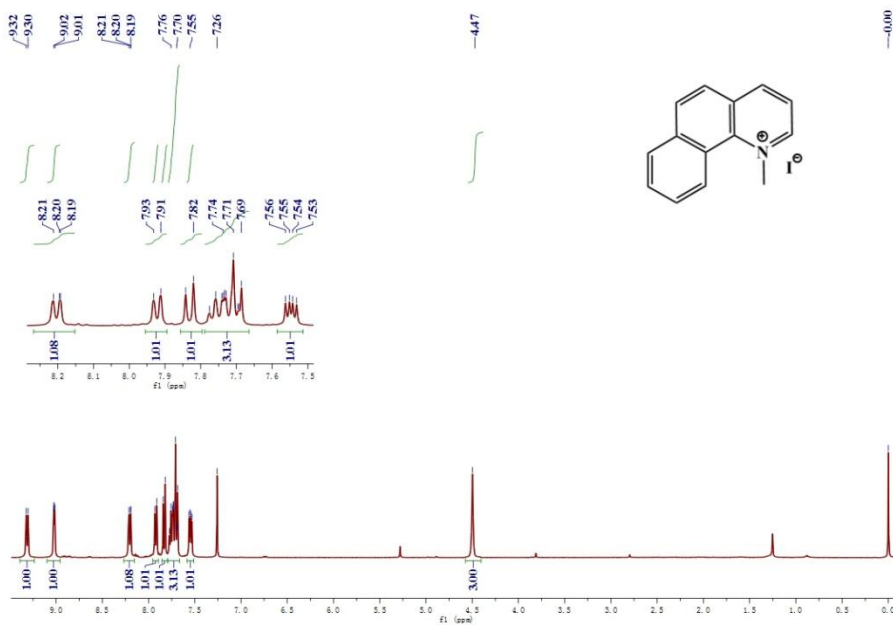


Figure S6. ^1H NMR of 1f in CDCl_3 (400 MHz), related to Table 2.

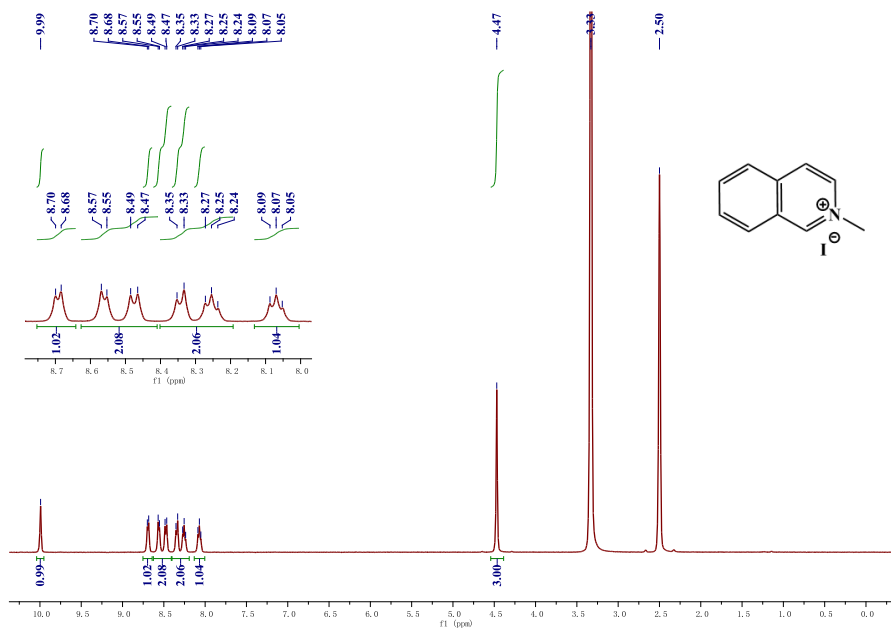


Figure S7. ^1H NMR of 3a in $\text{DMSO-}d_6$ (400 MHz), related to Table 2.

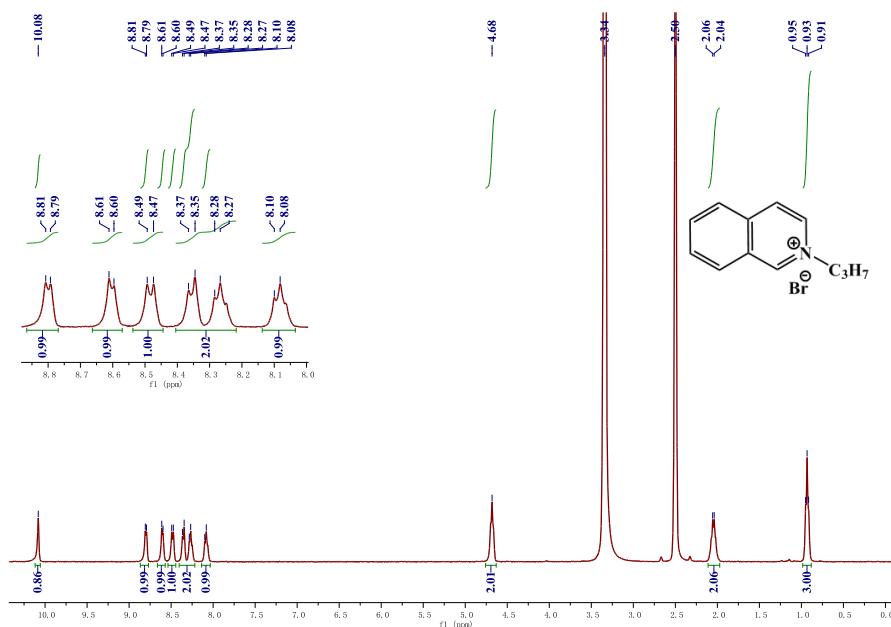


Figure S8. ^1H NMR of 3b in $\text{DMSO-}d_6$ (400 MHz), related to Table 2.

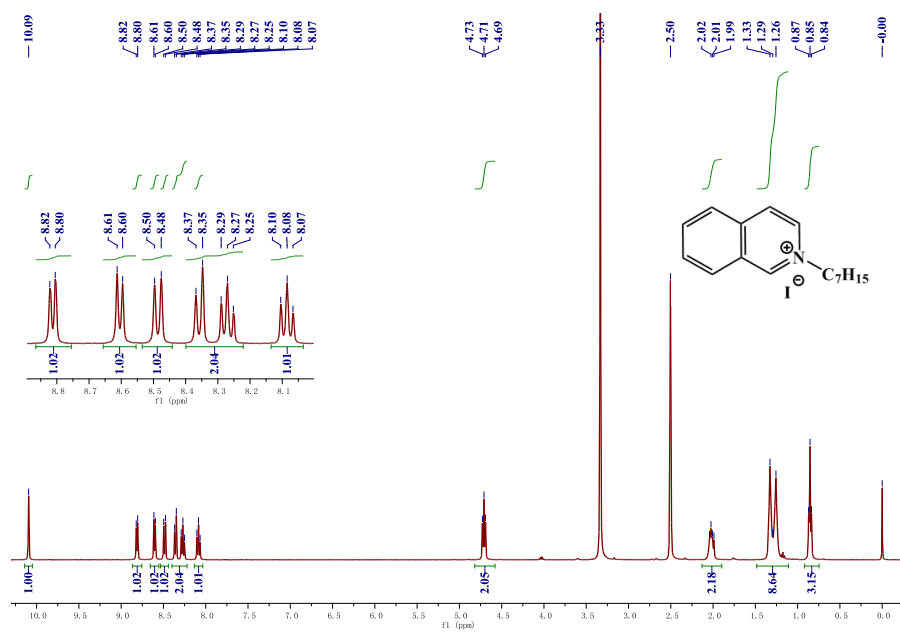


Figure S9. ^1H NMR of 3c in $\text{DMSO-}d_6$ (400 MHz), related to Table 2.

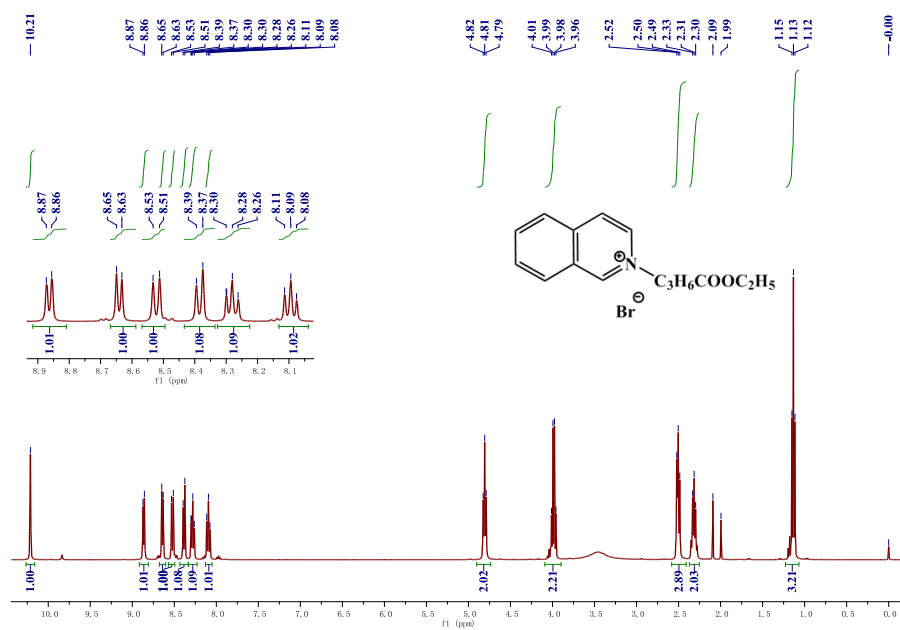


Figure S10. ^1H NMR of 3d in $\text{DMSO-}d_6$ (400 MHz), related to Table 2.

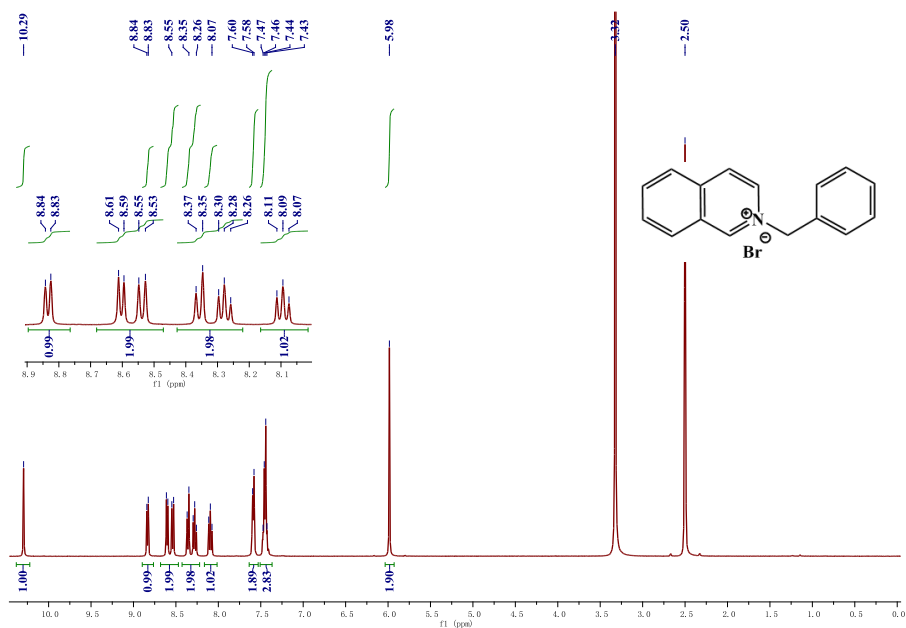


Figure S11. ^1H NMR of 3e in $\text{DMSO-}d^6$ (400 MHz), related to Table 2.

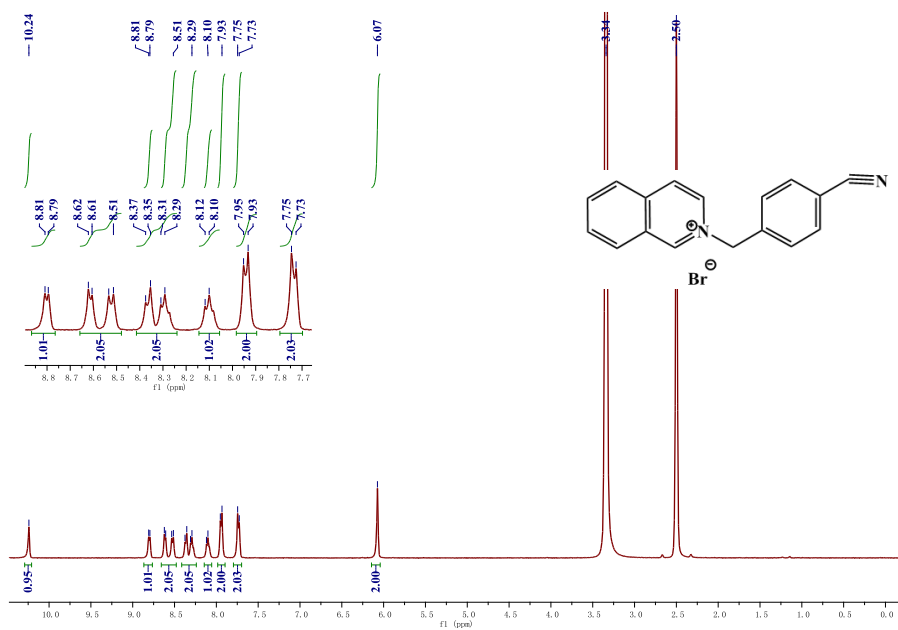


Figure S12. ^1H NMR of 3f in $\text{DMSO-}d^6$ (400 MHz), related to Table 2.

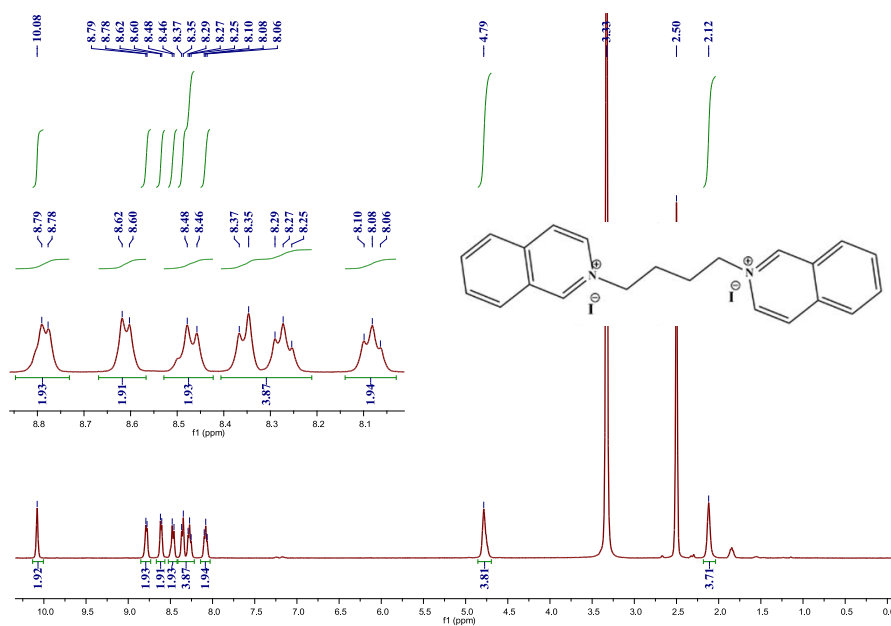


Figure S13. ¹H NMR of 3g in DMSO-*d*₆ (400 MHz), related to Table 2.

Supplementary figures for ¹H-NMR spectra of products 2a-2f and 4a-4g.

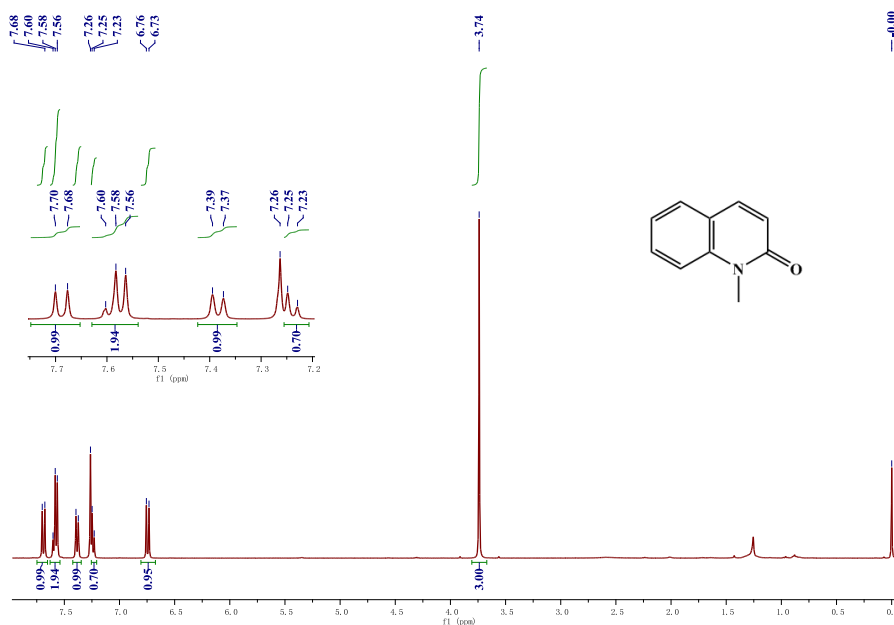


Figure S14. ¹H NMR of 2a in CDCl₃ (400 MHz), related to Table 1 and Table 2.

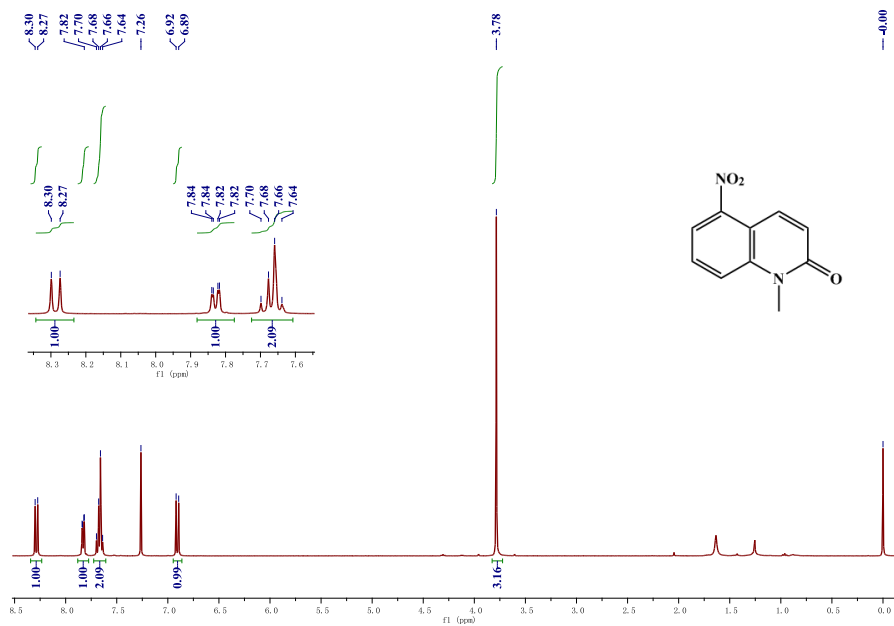


Figure S15. ¹H NMR of 2b in CDCl₃ (400 MHz), related to Table 2.

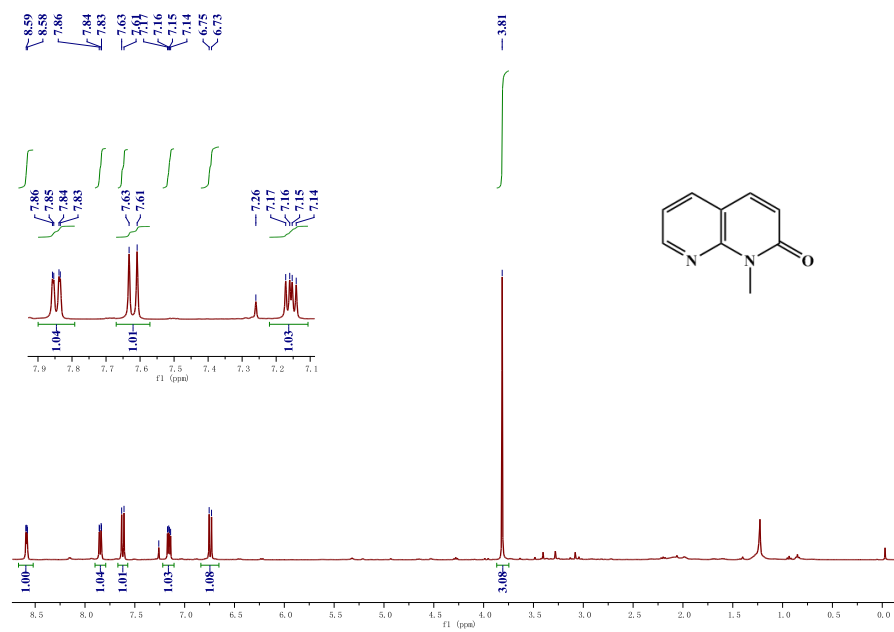


Figure S16. ¹H NMR of 2c in CDCl₃ (400 MHz), related to Table 2.

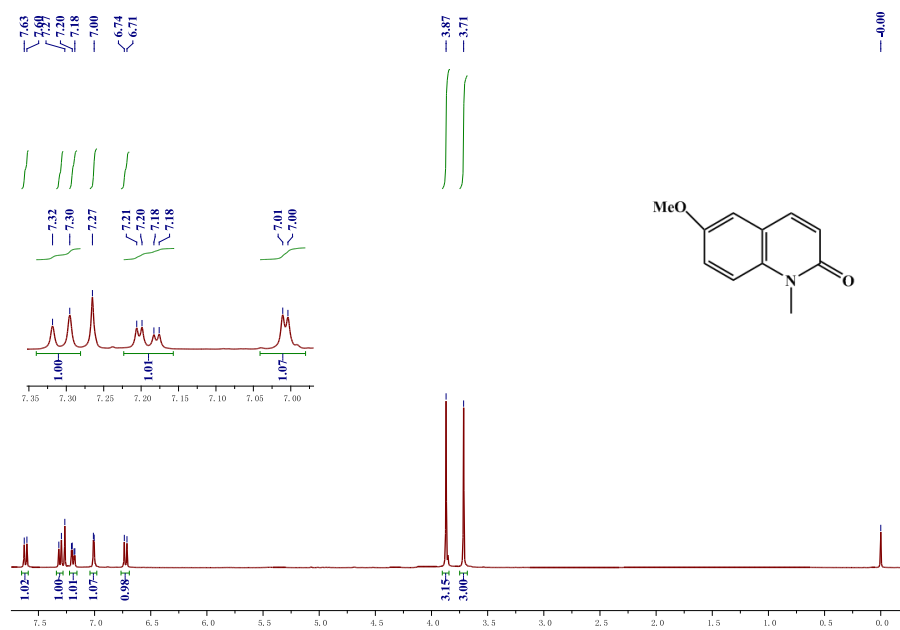


Figure S17. ^1H NMR of 2d in CDCl_3 (400 MHz), related to Table 2.

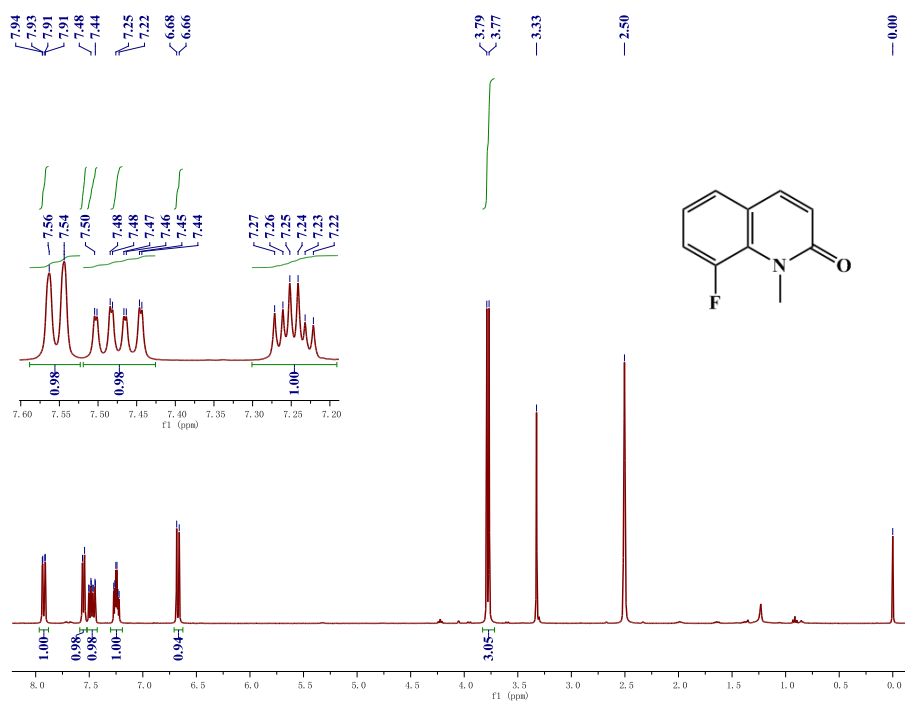


Figure S18. ^1H NMR of 2e in $\text{DMSO}-d_6$ (400 MHz), related to Table 2.

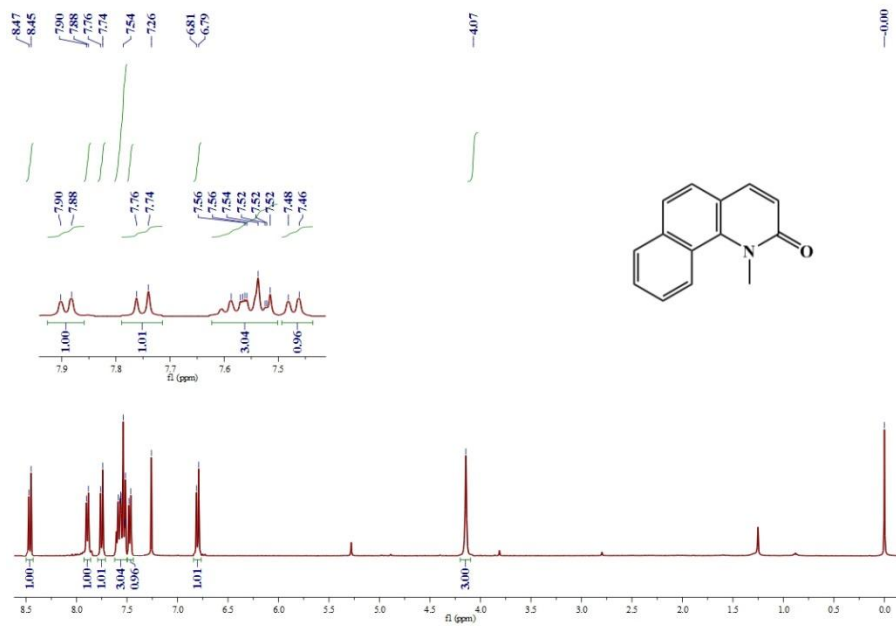


Figure S19. ^1H NMR of 2f in CDCl_3 (400 MHz), related to Table 2.

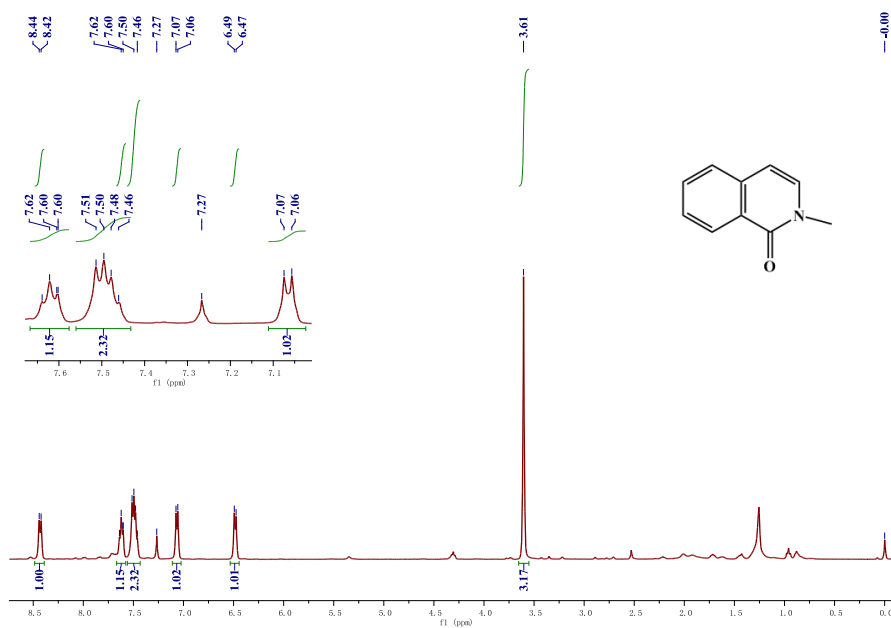


Figure S20. ^1H NMR of 4a in CDCl_3 (400 MHz), related to Table 2.

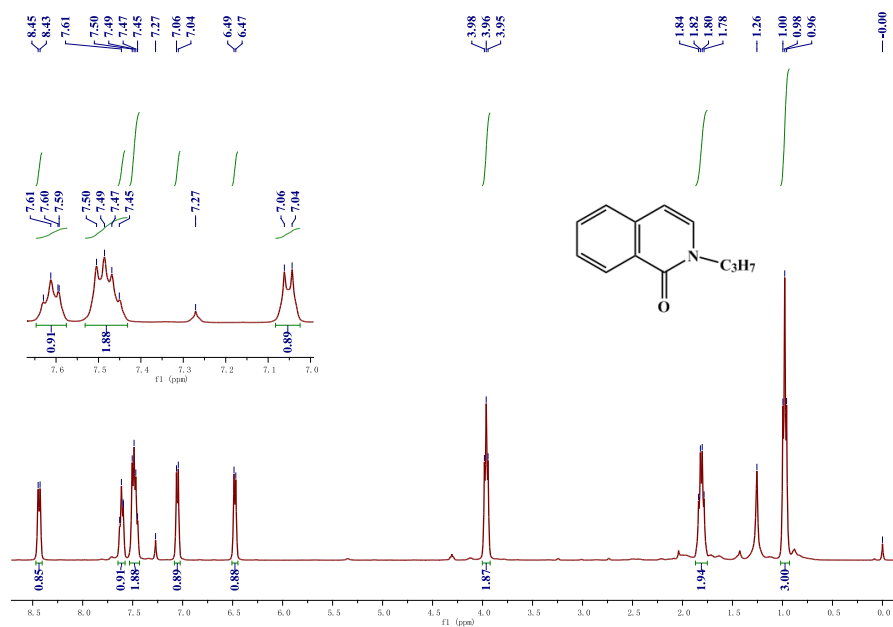


Figure S21. ^1H NMR of 4b in CDCl_3 (400 MHz), related to Table 2.

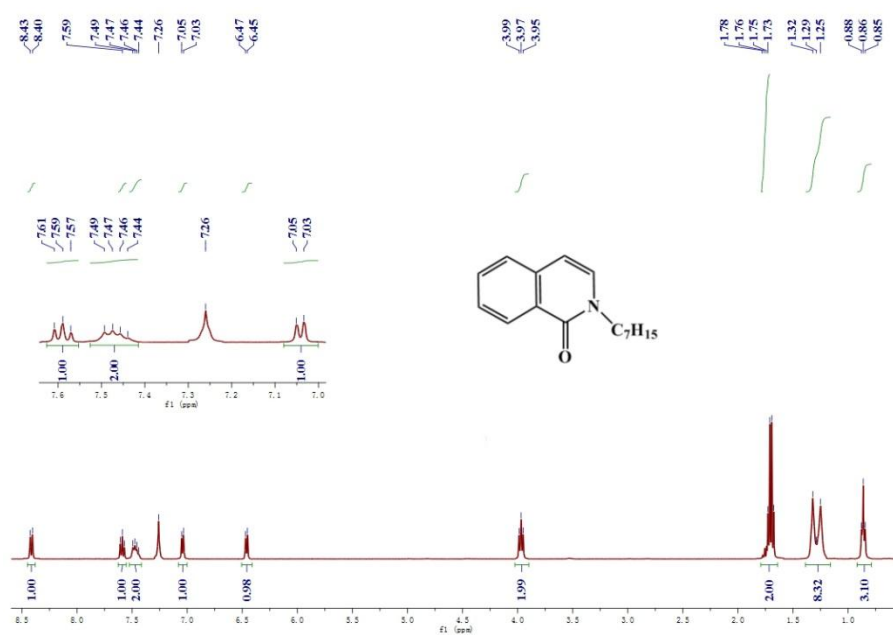


Figure S22. ^1H NMR of 4c in CDCl_3 (400 MHz), related to Table 2.

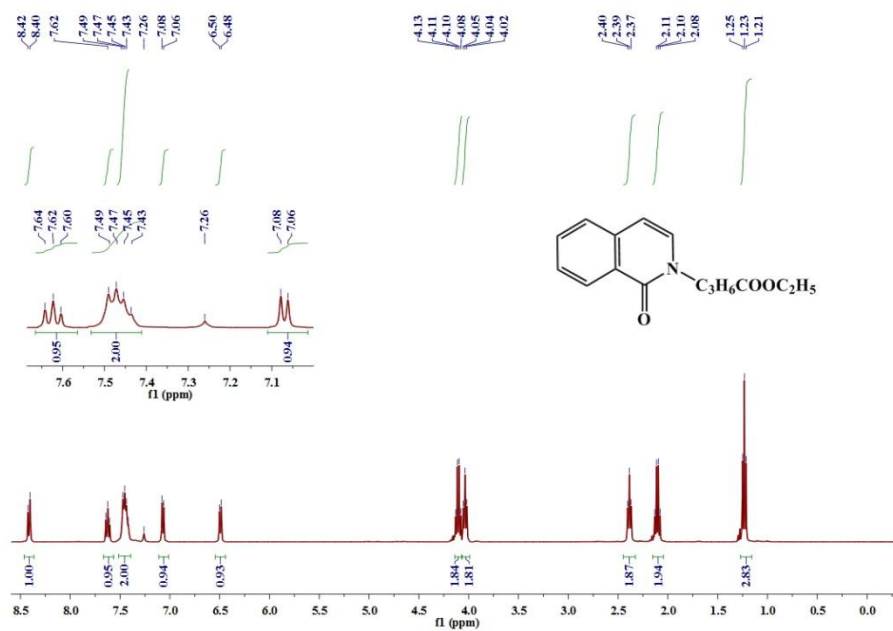


Figure S23. ^1H NMR of 4d in CDCl_3 (400 MHz), related to Table 2.

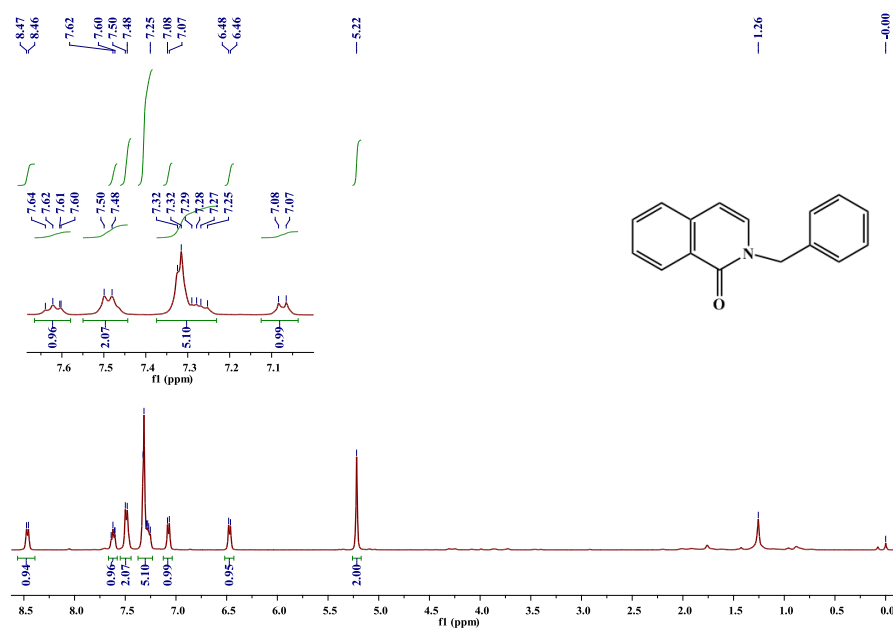


Figure S24. ^1H NMR of 4e in CDCl_3 (400 MHz), related to Table 2.

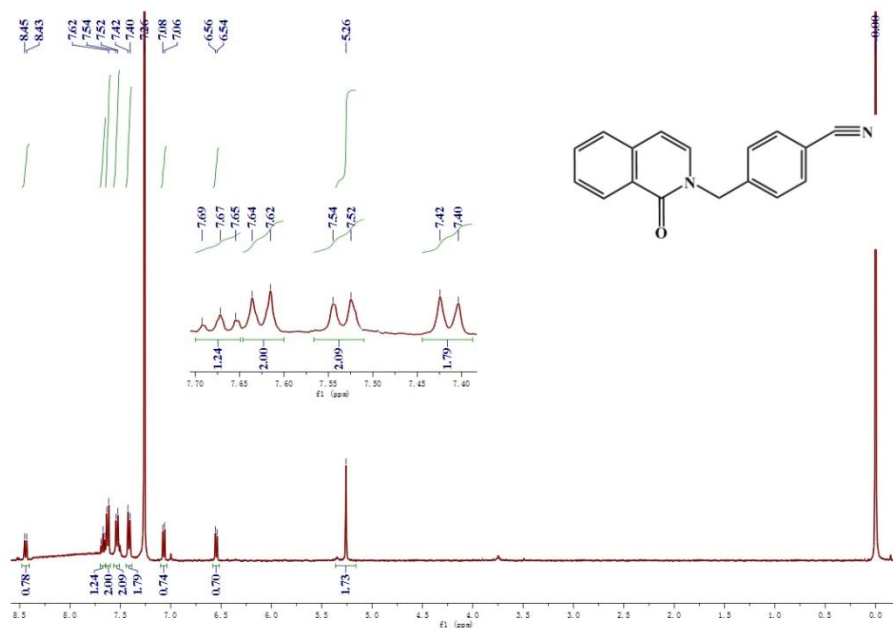


Figure S25. ¹H NMR of 4f in CDCl₃ (400 MHz), related to Table 2.

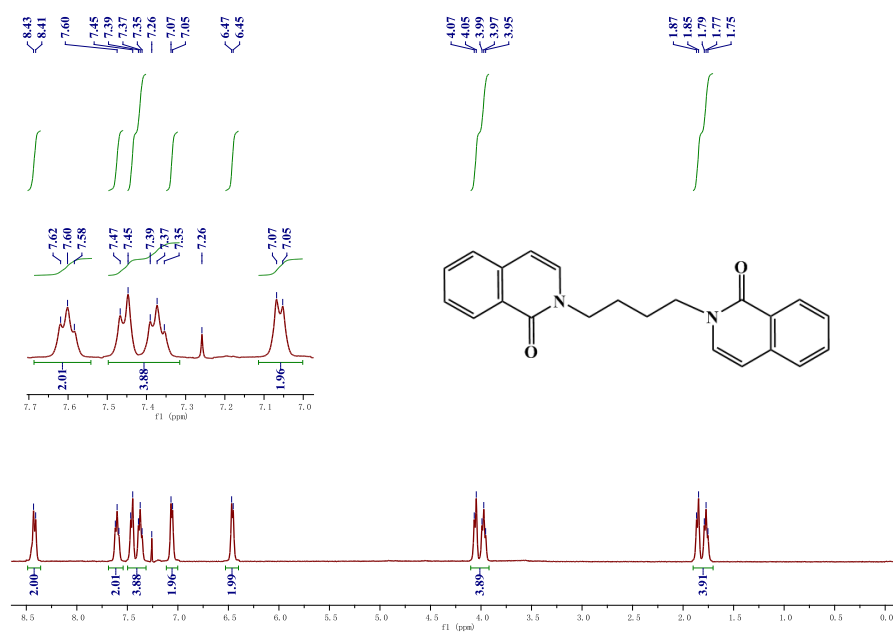


Figure S26. ¹H NMR of 4g in CDCl₃ (400 MHz), related to Table 2.

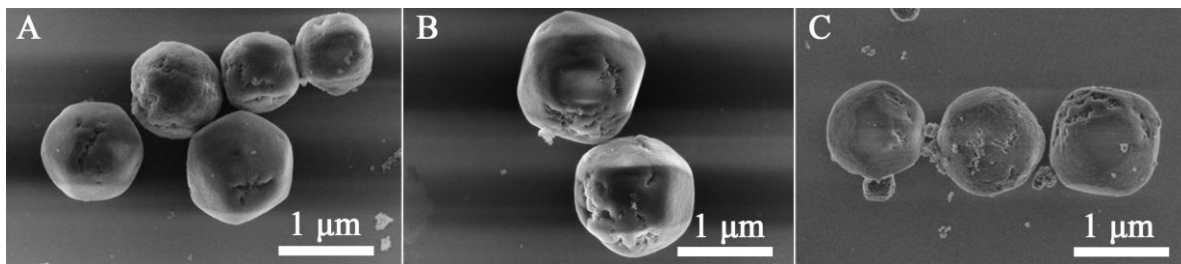


Figure S27. HRSEM images of PCN-221 and composite, related to Figure 1.

- (A) PCN-221,
- (B) Pt_{0.9}@PCN-221,
- (C) Pt_{0.9}@PCN-221 after catalytic reactions.

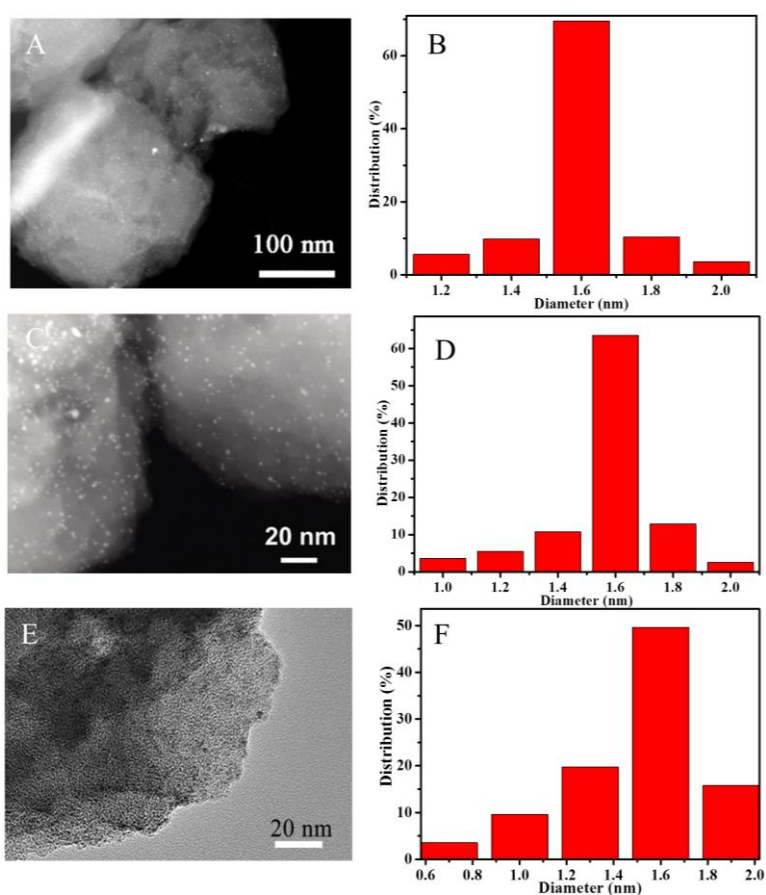


Figure S28. HRTEM images of Pt_{1.6}@PCN-221 (A, C, E) and the size distributions of the corresponding Pt NCs (B, D, F), 100 of NCs were counted to get the size distribution, related to Figure 1.

- (A) (C) HRTEM image of Pt_{1.6}@N-C,
- (B) (D) size distributions of Pt NCs in Pt_{1.6}@N-C composite obtained with five batches of samples.
- (E) HRTEM image of Pt_{1.6}@PCN-221,
- (F) size distributions of Pt NCs in Pt_{1.6}@PCN-221 composite.

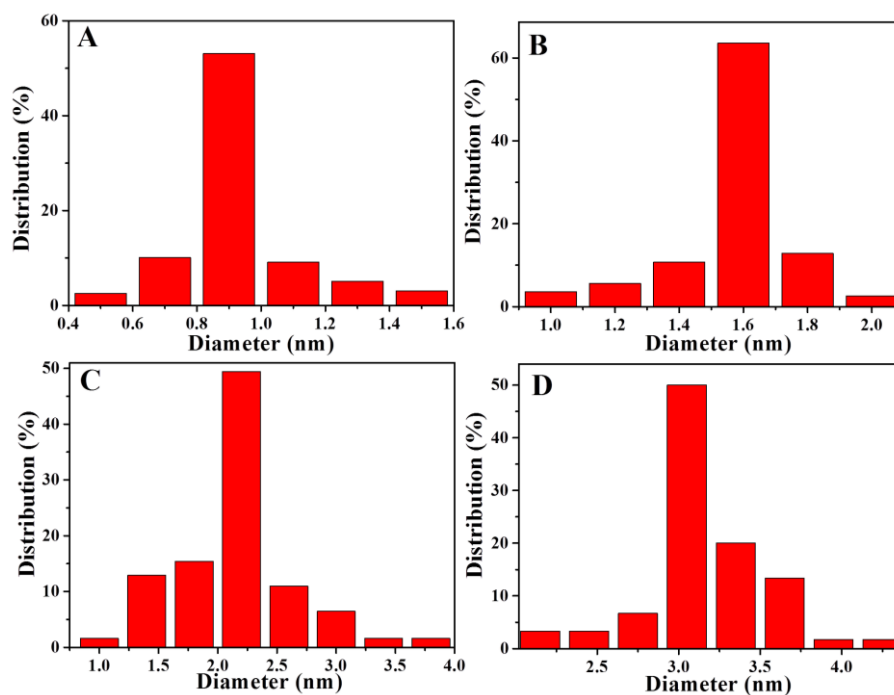


Figure S29. Size distributions of Pt NCs in Pt_x@N-C composites, 100 of NCs were counted to get the size distribution, related to Figure 1.

- (A) Pt_{0.9}@N-C,
- (B) Pt_{1.6}@N-C,
- (C) Pt_{2.2}@N-C,
- (D) Pt_{3.0}@N-C.

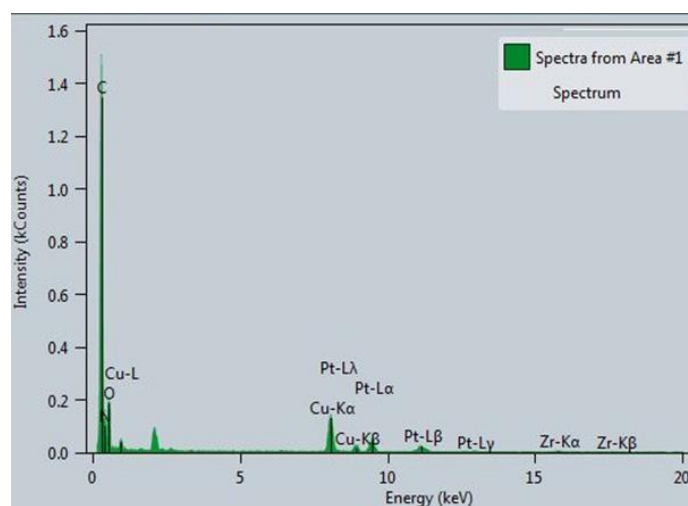


Figure S30. EDS analysis, related to Figure 1.

EDS analysis for Pt_{0.9}@N-C, indicating the obvious presence of Pt in the N-C support.

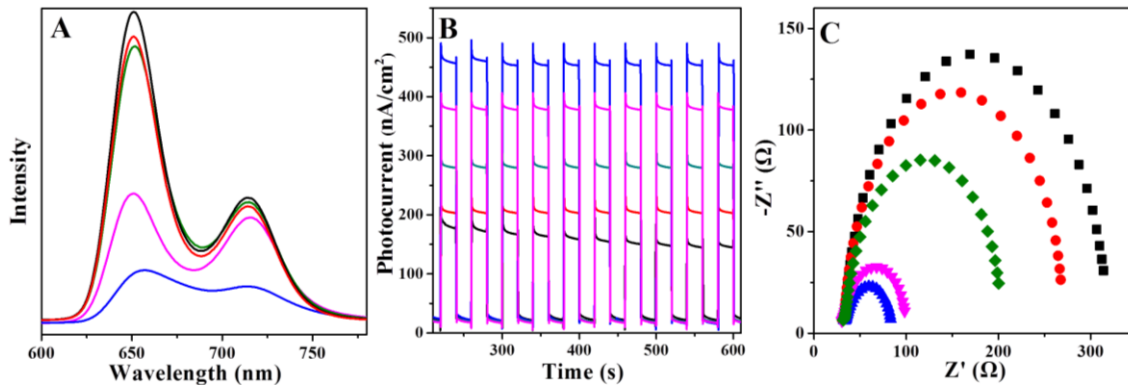


Figure S31. PL emission spectra analysis, Photocurrent responses analysis and EIS Nyquist plots analysis of the composite, related to Figure 2.

(A) PL emission spectra (excited at 410 nm),

(B) Photocurrent responses,

(C) EIS Nyquist plots for PCN-221 (black), Pt_{0.9}@PCN-221 (blue), Pt_{1.6}@PCN-221 (magenta), Pt_{2.2}@PCN-221 (red), and Pt_{3.0}@PCN-221 (olive).

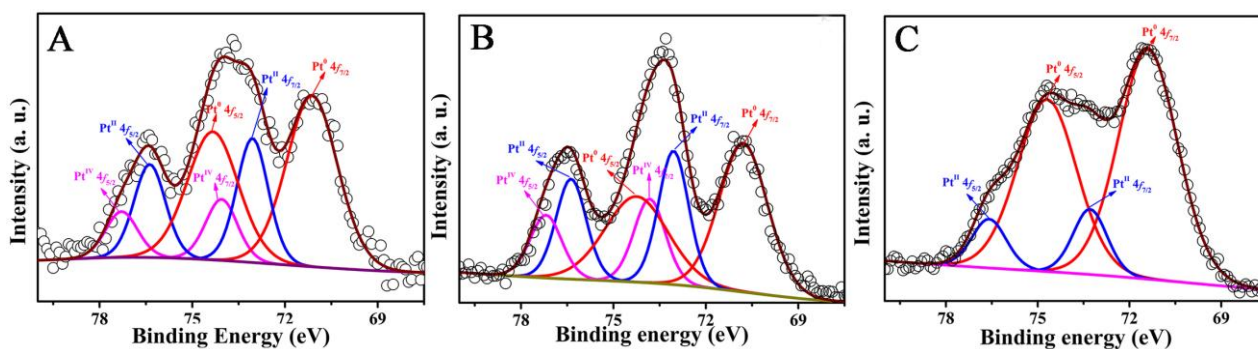


Figure S32. XPS spectra of Pt 4f, related to Figure 2.

(A) Pt_{0.9}@PCN-221,

(B) Pt_{1.6}@PCN-221,

(C) Pt_{3.0}@PCN-221.

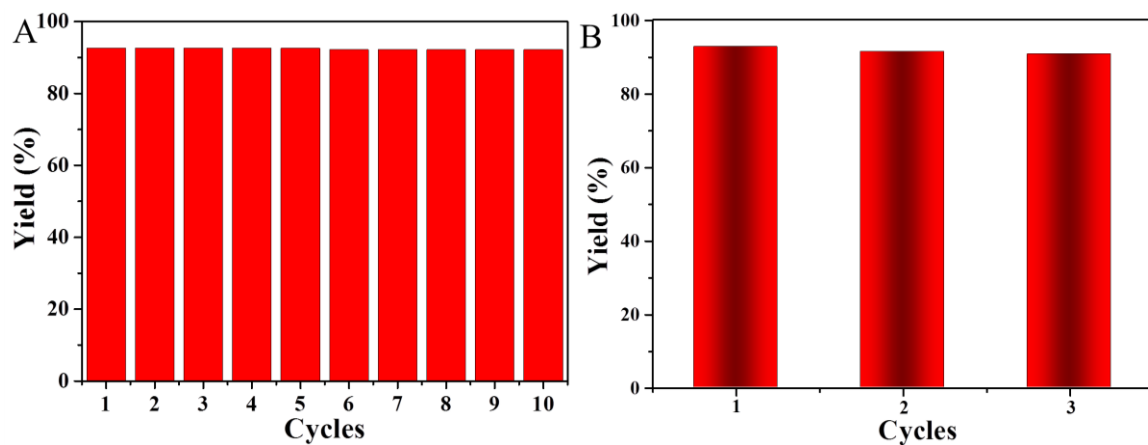


Figure S33. Photocatalytic recyclability, related to Figure 3.

(A) Recyclability of Pt_{0.9}@PCN-221 for photocatalytic oxidation of 1a.

(B) Recyclability of Pt_{0.9}@PCN-221 for photocatalytic oxidation of 1b in the gram-scale synthesis.

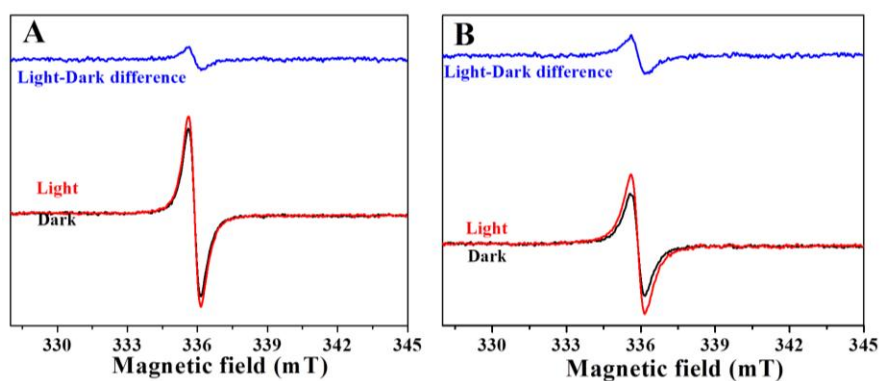


Figure S34. ESR spectra of porphyrin π -cation radicals, related to Figure 4.

(A) PCN-221,

(B) Pt_{0.9}@PCN-221.

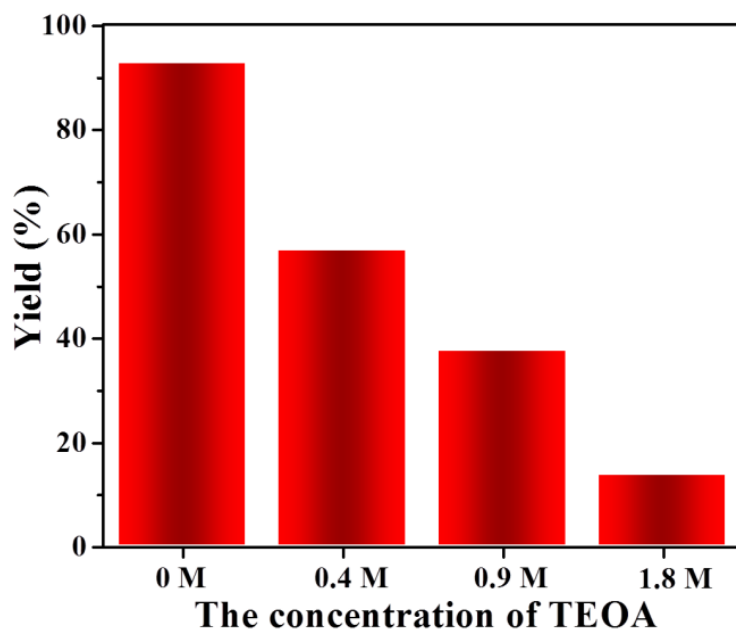


Figure S35. Photocatalytic experiments with different concentration of TEOA, related to Figure 4.

Photo-oxidation of 1a with Pt_{0.9}@PCN-221 as the catalyst by introducing different concentration of TEOA under visible-light irradiation.

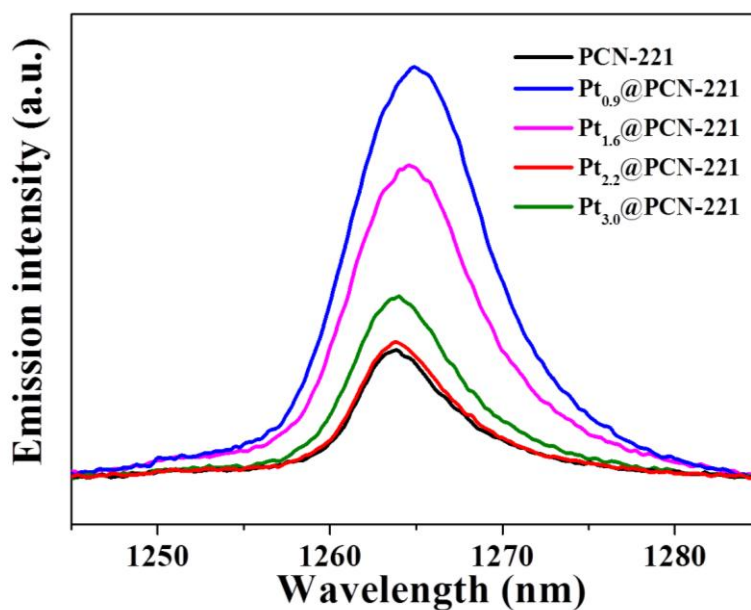


Figure S36. Phosphorescence spectra of singlet oxygen (¹O₂), related to Figure 4. Phosphorescence spectra of singlet oxygen (¹O₂) were detected in the presence of PCN-221 (black), Pt_{0.9}@PCN-221 (blue), Pt_{1.6}@PCN-221 (magenta), Pt_{2.2}@PCN-221 (red) and Pt_{3.0}@PCN-221(olive) with the excitation at 410 nm.

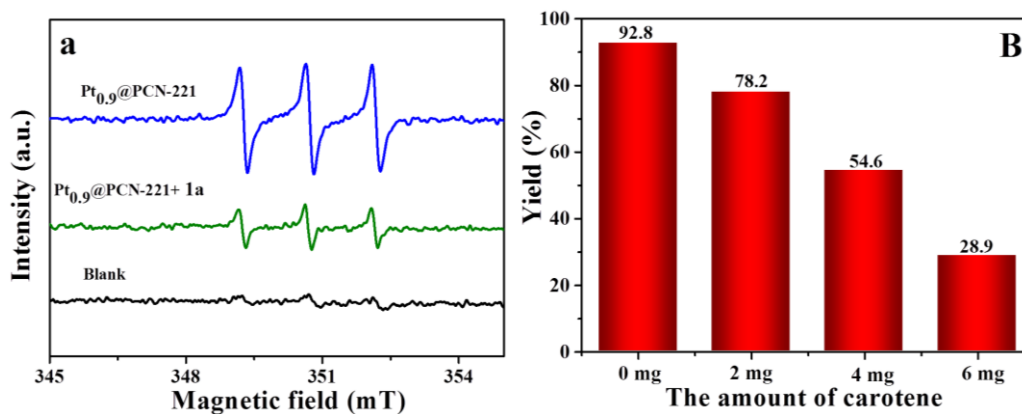


Figure S37. ESR spectra and photocatalytic experiments, related to Figure 4.

(A) ESR spectra of the mixture of 4-oxo-TMP and Pt_{0.9}@PCN-221 with/without 1a under visible-light irradiation.

(B) Photo-oxidation of 1a with Pt_{0.9}@PCN-221 as the catalyst by introducing different concentration of carotene under visible-light irradiation.

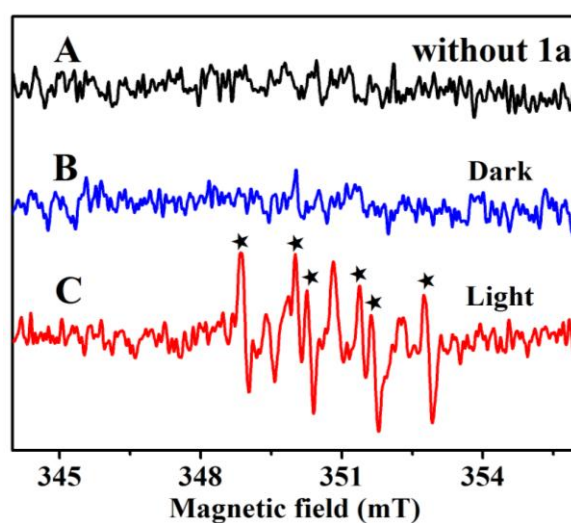


Figure S38. ESR spectra in DMSO, related to Figure 4.

(A) Pt_{0.9}@PCN-221, Cs₂CO₃ and DMPO (a spin-trapping agent) in the absence of 1a with the irradiation for 5 min;

(B) Pt_{0.9}@PCN-221, Cs₂CO₃, DMPO and 1a under dark for 5 min;

(C) Pt_{0.9}@PCN-221, Cs₂CO₃, DMPO and 1a with the irradiation for 5 min.

3. Supplementary Tables

Table S1. Surface area, N₂ uptake and pore volumes for Pt_x@PCN-221, related to Figure 1E.

Entry	BET surface area (m ² •g ⁻¹)	N ₂ uptake (STP cm ³ •g ⁻¹)	Pore volume (cm ³ •g ⁻¹) ^a
PCN-221	2002	459.97	0.9977
Pt _{0.9} @PCN-221	1867.2	429.01	0.9634
Pt _{1.6} @PCN-221	1819.9	418.13	0.8429
Pt _{2.2} @PCN-221	1545.6	355.11	0.8021
Pt _{3.0} @PCN-221	1182.8	271.74	0.5122

^ameasurements were taken at P/P₀ = 0.99.

Table S2. Visible-light driven aerobic oxidation of 1-methylquinoline iodide (1a) to 1-methyl-2-quinolinone (2a) with Pt_x@PCN-221 as catalysts^a, related to Table 1.

Entry	Catalyst	t/h	Yield/% ^b
1	Pt _{0.9} @PCN-221	2	93.5
2	Pt _{1.6} @PCN-221	2	80.2
3	Pt _{2.2} @PCN-221	2	55.3
4	Pt _{3.0} @PCN-221	2	14.6

^aReaction conditions: 1a (0.4 mmol), 0.075 mol% Pt vs. 1a for Pt_x@PCN-221, Cs₂CO₃ (0.6 mmol), THF (4 mL), air, room temperature, irradiation with 425 nm LED in a 5 mL glass tube.

^bIsolated yield.

Supplemental References:

Feng, D., Jiang, H.-L., Chen, Y.-P., Gu, Z.-Y., Wei, Z., and Zhou, H.-C. (2013). Metal–Organic Frameworks based on previously unknown Zr₈/Hf₈ cubic clusters. *Inorg. Chem.* *52*, 12661–12667.

Wu, C.-K., and Yang, D.-Y. (2016). Visible-light-mediated reaction: Synthesis of quinazolinones from 1,2- dihydroquinazoline 3-oxides. *RSC Adv.* *6*, 65988–65994.

Wang, G., Hu, W., Hu, Z., Zhang, Y., Yao, W., Li, L., Fu, Z., and Huang, W. W. (2018). Carbene-catalyzed aerobic oxidation of isoquinolinium salts: Efficient synthesis of isoquinolinones. *Green Chem.* *20*, 3302–3307.

Barfield, M., Walter, S. R., Clark, K. A., Gribble, G. W., Haden, K. W., Kelly, W. J., and Le Houllier, C. S. (1982). Proton, Carbon-13 and Fluorine-19 NMR studies of N-alkyl-8-fluoroquinolinium halides: Relative signs of through-space ¹H-¹⁹F and ¹³C-¹⁹F coupling constants. *Org. Magn. Reson.* *20*, 92.

He, A., Dong, B. X.-T., Feng, X.-T., and Yao, S. (2018). Extraction of bioactive ginseng saponins using aqueous two-phase systems of ionic liquids and salts. *Sep. Purif. Technol.* *196*, 270–280.